Chem

CellPress

Article

Switchable Interaction in Molecular Double Qubits

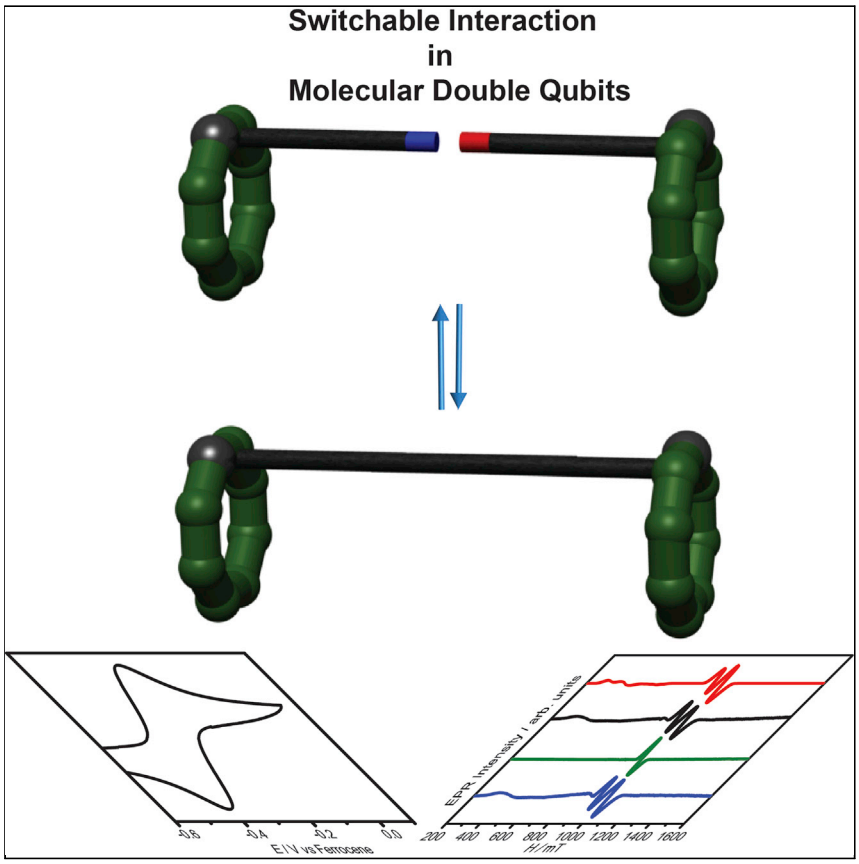

Winpenny and colleagues describe supramolecular systems where {Cr_7Ni} rings are used as qubits, linked by redox-switchable {Ru_2M} oxo-centered triangles (M = Zn, Ni, or Co). When M = Co, the molecular-based double-qubit assembly has the physical characteristics needed to implement the √iSWAP gate. The authors propose a local control of the qubit-qubit interaction on an individual supramolecular dimer, achieved by an STM tip. Detailed simulations show that many quantum gates can be concatenated for implementation of quantum simulation algorithms.

Jesús Ferrando-Soria, Samantha A. Magee, Alessandro Chiesa, ..., Grigore A. Timco, Eric J.L. McInnes, Richard E.P. Winpenny

richard.winpenny@manchester.ac.uk

HIGHLIGHTS

A family of switchable-exchange molecular double qubits has been obtained

Detailed simulations show that qubit-qubit interaction can be effectively switched

Many quantum gates can be concatenated for implementing quantum simulation algorithms

Ferrando-Soria et al., Chem 1, 727–752
November 10, 2016 Published by Elsevier Inc.
http://dx.doi.org/10.1016/j.chempr.2016.10.001

Chem

CellPress

Article

Switchable Interaction in Molecular Double Qubits

Jesús Ferrando-Soria,[1] Samantha A. Magee,[1] Alessandro Chiesa,[2] Stefano Carretta,[2] Paolo Santini,[2] Iñigo J. Vitorica-Yrezabal,[1] Floriana Tuna,[1] George F.S. Whitehead,[1] Stephen Sproules,[1,3] Kyle M. Lancaster,[4] Anne-Laure Barra,[5] Grigore A. Timco,[1] Eric J.L. McInnes,[1] and Richard E.P. Winpenny[1,6,*]

SUMMARY

Quantum information processing (QIP) could revolutionize how we simulate and understand quantum systems. Any QIP scheme requires both individual units (qubits) that have long phase memories and switchable units that can be placed between the qubits. Here, we describe supramolecular systems where {Cr_7Ni} rings are used as qubits, linked by redox-switchable {Ru_2M} oxo-centered triangles (M = Zn, Ni, or Co). The supramolecular assemblies have been structurally characterized and involve two {Cr_7Ni} rings bound to {Ru_2M} triangles through *iso*-nicotinate ligands. Detailed physical studies, including electrochemistry and electron paramagnetic resonance spectroscopy, show that when M = Co, the supramolecular assembly has the physical characteristics needed to implement the √iSWAP gate, which is an important entangling two-qubit gate. Detailed simulations show that the fidelity of this gate is potentially very high and depends on the phase memory time of the {Cr_7Ni} qubits but not the {Ru_2Co} switch.

INTRODUCTION

Several groups have proposed that paramagnetic molecules could be used as qubits, the basic unit for the physical implementation of quantum information processing (QIP).[1,2] The first significant proposal was from Leuenberger and Loss[3] and involved using the lowest energy multiplet of an {Mn_{12}} single-molecule magnet.[4] However, much more research has been devoted to studies of two-level systems,[5,6] which are normally S = 1/2 molecules, which could be organic radicals,[7,8] centers within polyoxometallates[9] and other metal cage complexes,[10] or simple coordination complexes.[11–16] Other two-level systems studied include the ground m_J doublet of anisotropic lanthanide ions.[17,18]

Implementing interesting quantum algorithms requires qubits with long-lived coherent superposition states. A measurement of the robustness of a qubit against decoherence is provided by both the spin-lattice relaxation time (T_1) and the phase memory time (T_M), which must be much longer than the time required for the quantum operations. The finite value of T_1 arises from spin-phonon interactions and usually shows pronounced temperature dependence. Conversely, the irreversible T_M originates from pure dephasing mechanisms induced by the dynamic interaction of the electron spins with the magnetic nuclei and by flip-flop processes associated to intermolecular dipolar couplings.

Molecules present distinct challenges when compared with other systems that have been proposed as qubits.[19–21] First, as individual units, molecular

The Bigger Picture

One of the greatest potential advantages of quantum information processing (QIP) over classic computing is the efficient simulation of the behavior of quantum systems. Many physical systems have been studied for QIP, and each has advantages and disadvantages. The use of supramolecular chemistry for QIP allows us to design architectures and interactions that are entirely controllable through chemistry. If such schemes could be made to work, the implications are a far better understanding of quantum systems. In addition, certain computational tasks such as searching unsorted directories or factoring large numbers into primes could be performed much more quickly.

Table 1. Phase Memory Times for Some Representative Molecular Qubits

Compound[a]	T (K)	T_M (μs)[b]	Reference
$[CrNi_2(\mu_3\text{-}F)(piv)_6(Hpiv)_3]$		0.64	Walsh et al.[10]
$[Cu^{II}(pc)]$	5	2.6	Warner et al.[11]
	80	1.0	
$[Ru^{III}(ox)_3]^{3-}$[c]	5	3.44	Graham et al.[12]
$[Os^{III}(CN)_6]^{3-}$[d]	5	4.12	Graham et al.[12]
$(Ph_4P)_2[Cu^{II}(mnt)_2]$	7	9.0	Bader et al.[13]
	100	7.0	
$(Ph_4P)_2[V^{V}(dbmit)_3]$	10	675	Zadrozny et al.[14]
	120	1.18	
$(Ph_4P)_2[V^{V}(\beta\text{-}dmit)_3]$	10	2.87	Zadrozny et al.[14]
	120	0.59	
$(Ph_4P)_2[V^{V}(dmit)_3]$	10	2.59	Zadrozny et al.[14]
	120	0.57	
$(Ph_4P)_2[V^{V}(dmito)_3]$	10	2.79	Zadrozny et al.[14]
	120	0.64	
$[V^{IV}O(pc)]$	4.3	3.41	Atzori et al.[15]
	150	2.04	
[Yb(saltren)]	5	0.5	Pedersen et al.[16]
$[CeEr(HL)_2(H_2L)(NO_3)(py)(H_2O)]$	5	0.4	Aguilà et al.[18]
$Cs[Cr^{III}_7NiF_8(d\text{-}piv)_6$	1.5	15.3	Wedge et al.[22]
	5	0.89	
$[Ho(W_5O_{18})_2]^{9-}$	5	8.4	Shiddiq et al.[24]

[a]Ligand abbreviations: Hpiv, pivalic acid; H_2pc, phthalocyanine; ox, oxalate; mnt, maleonitriledithiolato; dbmit, 2,5-dithioxobenzo[1,2- d:3,4-d']bis[1,3]dithiolene-7.8-dithiolate; β-dmit, 1,2-dithiolane-3-thione-4,5-dithiolate; dmit, 1,3-dithiolane-2-thione-4,5-dithiolate; dmito, 1,3- dithiolane-2-one-4,5-dithiolate; saltren, tris(2-ethylsalicylideneimine)amine; H_3L, 6-(3-oxo-3-(2-hydroxyphenyl)propionyl)pyridine-2-carboxylic acid; and *d*-piv, deuterated pivalate.
[b]T_M represents the phase memory time.
[c]M = Fe^{III} (1.83); Cr^{III} (2.79).
[d]M = Fe^{III} (2.38); Ru^{III} (2.55).

qubits might not have phase memory times as long as those of other quantum systems, and hence performing multiple operations on molecular electron spin qubits could be challenging. Extensive studies of the phase memory times have shown the importance of the electron-nuclear hyperfine interaction;[11–16,22] attempts have been made to minimize the number of protons in the structure and to limit the elements present that have a significant nuclear magnetic moment.[13–15] This has led to T_M as long as 0.7 ms at 10 K[14] and 1 μs at room temperature.[13,15] Other successful approaches have involved using complex pulse sequences[23] and, very recently, the use of clock transitions with a monometallic holmium complex.[24] Thus, there have been considerable advances in improving phase memory times through intelligent chemical design since the initial measurements that established the feasibility of using molecules in this context (Table 1).[25] Second, molecules are not as compatible with the integrated circuits used in information processing as nanostructures created by lithography. There is a growing body of work studying the addressing of spins in individual molecules,[26–31] but this is still a developing field.

[1]School of Chemistry and Photon Science Institute, The University of Manchester, Oxford Road, Manchester M13 9PI, UK

[2]Dipartimento di Fisica e Scienze della Terra, Università di Parma, Parco Area delle Scienze 7/a, 43124 Parma, Italy

[3]WestCHEM, School of Chemistry, University of Glasgow, Glasgow G12 8QQ, UK

[4]Baker Laboratory, Department of Chemistry and Chemical Biology, Cornell University, Ithaca, NY 14853, USA

[5]Laboratoire National des Champs Magnétiques Intenses, CNRS UPR 3228, Université J. Fourier, 25 Avenue des Martyrs, B.P. 166, 38042 Grenoble Cedex 09, France

[6]Lead Contact

*Correspondence: richard.winpenny@manchester.ac.uk

http://dx.doi.org/10.1016/j.chempr.2016.10.001

An advantage of molecules is that molecular qubits could be brought together with great control into arrays using the flexibility and richness of supramolecular chemistry,[32–34] and hence two-qubit quantum gates (QGs) could be implemented efficiently. The analog between supramolecular chemistry and the requirements of QIP is quite strong: in both cases, we wish to bring together individual units while requiring them to both retain their original identities and interact in a controlled manner with other units. This richness has led to theoretical proposals where complex chemical structures could be used to produce quantum simulators.[35]

We have proposed using {Cr_7Ni} heterometallic rings as qubits[36] because they are two-level systems that meet criteria required for qubits, e.g., they have sufficient phase memory times to allow many gate operations before state degradation can occur.[22,25] To this point, we have built assemblies where functionalized {Cr_7Ni} rings were linked by coordination to different central nodes,[37–39] without altering their intrinsic physical properties, and obtained a coherent coupling between the spins in some of them.[37,39]

Single-qubit rotations have also been demonstrated in several molecular systems, including {Cr_7Ni} rings.[40] The next step in producing a viable scheme for QIP with molecules is to perform entangling two-qubit QGs. The physical implementation of both single and two-qubit gates requires inter-qubit interactions to be turned on and off effectively. To date, this has provided a major experimental challenge. Two-qubit CNOT gates have been implemented only on pairs of permanently coupled qubits, such as *g*-engineered organic radicals[8] or lanthanide ions with very different *g* values.[18] In these schemes, the interaction between two dissimilar qubits produces a splitting in the low-lying two-qubit states to allow a single transition to be selectively addressed by means of resonant electron paramagnetic resonance (EPR) pulses. Thanks to this splitting, the excitation of the target depends on the state of the control, and the CNOT gate is implemented. However, the always-on qubit-qubit interaction induces an unwanted two-qubit evolution of the wave function, which must be corrected with proper sequences of pulses. This makes the scalability of this setup tricky.

Recently, we have proposed using a magnetic ion interposed between a pair of {Cr_7Ni} qubits and then dynamically switching the qubit-qubit interaction by a conditional excitation of the switch (depending on the state of the two qubits) by means of uniform magnetic pulses applied to a bulk crystal of nanomagnets.[37] In this proposed scheme, the physical interaction is never switched on or off, but still the induced dynamics are equivalent to those of interacting or non-interacting qubits.[37] These compounds are suitable for the implementation of the entangling controlled Z gate.[37]

Another very important entangling QG is the $\sqrt{\text{iSWAP}}$ gate, which brings a two-qubit product state into a superposition involving partial swapping the qubit states, i.e., $|01\rangle$ too $(|01\rangle + i|10\rangle)/\sqrt{2}$. The physical implementation of a sequence of $\sqrt{\text{iSWAP}}$ gate and of single-qubit rotations requires the presence of a switchable linker to turn on and off the interaction between qubits.

Here, we report studies of a series of redox-active mixed-metal pivalate triangles with the general formula $[Ru^{III}_2M^{II}O(O_2C^tBu)_6(py)_3]$ (M = Zn **2a**, Ni **2b**, and Co **2c**). We then use these oxo-centered triangles to link together molecular spin qubits, $[^nPr_2NH_2]$ $[Cr_7NiF_8(O_2C^tBu)_{15}(O_2C\text{-}Py)]$ **1** (abbreviated as {Cr_7Ni-O_2C-py}, where O_2C-py = *iso*-nicotinate) (Figure 1). This produces two-qubit assemblies with the

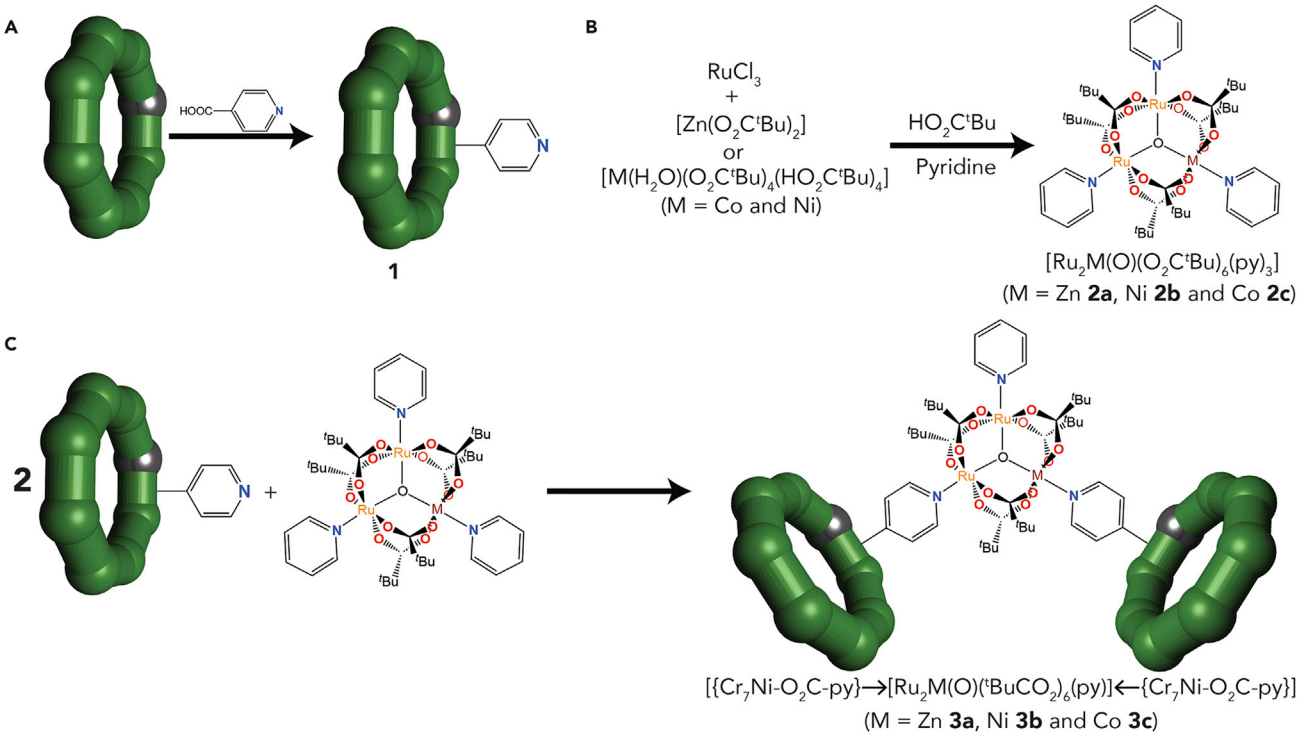

Figure 1. Modular Design Strategy for the Construction of Two-Qubit Assemblies

(A and B) Preparation of (A) *N*-pyridine functionalized {Cr_7Ni} rings (**1**) and (B) pivalate-bridged oxo-centered, mixed-metal triangular clusters $[Ru^{III}_2M^{II}O(O_2C^tBu)_6(py)_3]$ (M = Zn **2a**, Ni **2b**, and Co **2c**).

(C) Their linkage to give the corresponding dimeric ring assemblies $[\{Cr_7Ni\text{-}O_2C\text{-}py\}\rightarrow[Ru^{III}_2M^{II}O(O_2C^tBu)_6(py)]\leftarrow\{Cr_7Ni\text{-}O_2C\text{-}py\}]$ (M = Zn **3a**, Ni **3b**, and Co **3c**).

general formula $[\{Cr_7Ni\text{-}O_2C\text{-}py\}\rightarrow[Ru^{III}_2M^{II}O(O_2C^tBu)_6(py)]\leftarrow\{Cr_7Ni\text{-}O_2C\text{-}py\}]$ (M = Zn **3a**, Ni **3b**, and Co **3c**), in which two of the terminal pyridine ligands of the central triangle are replaced by the *iso*-nicotinate group of the two {Cr_7Ni-O_2C-py} (**1**)[39] rings.

Complexes **3a–3c** contain two very weakly interacting qubits with the potential to switch the inter-qubit interaction through the electrochemistry of the linking triangle, and we have studied the electrochemistry and EPR spectroscopy of these complexes.

Compound **3c** shows especially appealing physical properties for implementing the √iSWAP gate by means of a local electric control of the qubit-qubit interaction, which would involve manipulating the redox state of the link by means of a scanning tunneling microscope (STM) tip at the appropriate potential, along the lines of Lehmann et al.[9] This would switch the qubit-qubit interaction on and off, and implementing this experiment is extremely challenging. Here, we performed detailed simulations using experimental parameters obtained from EPR spectroscopy to demonstrate how such a gate would operate. We included the effect of decoherence in these simulations, which showed a very high fidelity for the implementation of the √iSWAP gate with the parameters measured for **3c**. This led us to propose **3c** as the elementary unit of a digital quantum simulator;[35] as a proof of principle, we report the quantum simulation of a Heisenberg model and find very good agreement with the expected evolution. The use of electrical fields has also been proposed to change the chirality of {Cu_3} triangles, as suggested by Trif et al.[41]

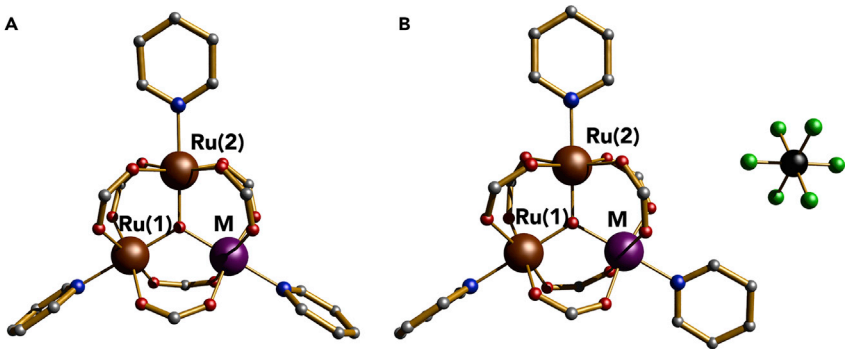

Figure 2. X-Ray Crystal Structures for 2a–2c and $2b^{ox}$–$2c^{ox}$

(A) Perspective view of **2a**–**2c** with labeling of metal atoms.

(B) Perspective view of $2b^{ox}$ and $2c^{ox}$ with labeling of metal atoms shows the PF_6^- counteranion.

Color code: M, purple; Ru, brown; N, cyan; O, red; C, gray; P, black; and F, pale green. H atoms and *tert*-butyl groups are omitted for clarity. Please note that the position of the statistically disordered M atom has been arbitrarily assigned.

RESULTS AND DISCUSSION

Syntheses

Full details are given in the Experimental Procedures and the Supplemental Information (Tables S9–S12). Compounds **2a**–**2c** were prepared from the reaction of a dinuclear ruthenium(III) precursor, $[Ru_2O(O_2C^tBu)_2]^{2+}$,[42,43] which was made in situ, with either $[Zn(O_2C^tBu)_2]$[44] or $[M_2(H_2O)(O_2C^tBu)_4(HO_2C^tBu)_4]$ (M = Ni^{II} or Co^{II}).[45] The reaction becomes purple, which indicates the formation of oxo-centered, mixed-metal trinuclear cages. These were isolated after several steps of purification for the removal of unreacted metal pivalate and excess pivalic acid. X-ray quality crystals of **2a**–**2c** were obtained by recrystallization from pyridine. In an alternative procedure, **2a**–**2c** could be obtained in higher yields (80%–90%) through the carboxylate substitution of the known oxo-centered mixed-metal acetate derivatives[46–49] by refluxing in excess pivalic acid and recrystallization from pyridine.

The corresponding one-electron oxidized complexes $2a^{ox}$–$2c^{ox}$ could be easily obtained from the reaction of **2a**–**2c** with $[FeCp_2](PF_6)$ in CH_2Cl_2 under nitrogen, and they were isolated as their hexafluorophosphate salts. X-ray quality crystals were just obtained for $2b^{ox}$ and $2c^{ox}$ from recrystallization from CH_2Cl_2/hexane.

The reaction of 2 equiv of **1** with 1 equiv of **2a**–**2c** in acetone yielded X-ray quality crystals of **3a**–**3c** after the reaction was left to stand for 1 week at room temperature. This reaction also worked with $2a^{ox}$–$2c^{ox}$, producing the corresponding one-electron oxidized assemblies $3a^{ox}$–$3c^{ox}$, which were isolated as their hexafluorophosphate salts.

X-Ray Crystal Structures

Mixed-Metal Triangular Clusters

2a crystallized in the hexagonal space group $P6_122$ with two-thirds of a molecule per asymmetric unit, whereas **2b** and **2c** crystallized in the monoclinic space group $P2_1/n$ with two molecules per asymmetric unit, one orthogonal to the other. They have the classic molecular structure of basic metal carboxylates triangles[50] with bridging pivalate and terminal pyridine groups (Figures 2A and S1). Because the metal ions are statistically disordered over the three sites, it was not possible to identify the position of the divalent metal ion within the triangular M_3O units, a common outcome in mixed-metal or mixed-valent triangular clusters.[50]

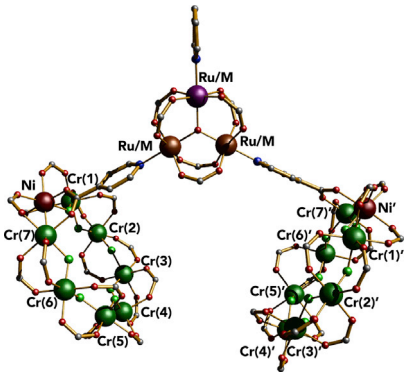

Figure 3. X-Ray Crystal Structures for 3a–3c
Molecular structure of **3a**–**3c** with labeling of metal atoms (symmetry code: (*l*) = *x*, *x* − *y*, 1/6 − *z*). Color code: M, purple; Cr, green; Ni, dark red; Ru, brown; N, cyan; O, red; C, gray; and F, pale green. $^{n}Pr_2NH_2^+$ cations are not shown. H atoms and *tert*-butyl groups are omitted for clarity.

The metal ions in **2a**–**2c** have a six-coordinate, octahedral MO_5N environment formed by four carboxylate oxygen atoms from the bridging pivalate ligands in the equatorial plane, and the central oxide and one nitrogen atom from pyridine groups occupy the axial positions. The three metals ions are positioned at the corners of an isosceles triangle with a mean separation of 3.301(5) (**2a**), 3.306(4) (**2b**), and 3.309(4) Å (**2c**). The central oxide lies within the M_3 plane of the metal atoms, whereas the six pivalate bridging ligands lie above and below the M_3O plane, and the pyridine N donors rest in two different orientations: one co-planar to the metal triangle and the other two perpendicular to this plane (Figure 2A and Table S1).

2b^{ox} and **2c**^{ox} are isostructural and crystallize in the triclinic *P*-1 space group. The structure consists of one cationic pivalate-bridged oxo-centered triangular cluster together with a hexafluorophosphate anion and a molecule of CH_2Cl_2 per asymmetric unit (Figures 2B and S2). The monoxidized cationic unit of **2b**^{ox} is very similar to **2b** but has small differences in bond lengths and angles (Table S1). In contrast, when compared with **2c**, complex **2c**^{ox} shows a considerable reduction in both the M–O_{piv} and M–N distances of 2.055(8)/2.010(7) and 2.153(6)/2.093(5) Å (**2c**/**2c**^{ox}), respectively (Table S1). The observed bond length shrinkage (averaged because of the statistical disorder) suggests a spin change from high-spin Co^{II} to low-spin Co^{III} upon oxidation. Unlike in **2b** and **2c**, two of the terminal pyridine groups lie parallel to the triangular plane of the complex instead of one.

Dimeric Ring Assemblies

Complexes **3a**–**3c** crystallize in the hexagonal $P6_122$ space groups. Their molecular structure consists of two symmetry-related {Cr_7Ni-O_2C-py} rings linked through the *iso*-nicotinate groups to the central [$Ru^{III}_2M^{II}O(^{t}BuCO_2)_6$(py)] (M = Zn **3a**, Ni **3b**, and Co **3c**) cluster (Figures 3 and S4). Once again, it was not possible to identify the position of the divalent metal ion within the central triangle because the metal ions are statistically disordered over the three sites.

The {Cr_7Ni-O_2C-Py} units in these assemblies contain an octagon of metal centers, where each internal edge is bridged by a fluoride and each external edge is bridged by two carboxylates. On seven edges, there are two pivalates, and on the eighth edge, there is one pivalate and one *iso*-nicotinate ligand; the Ni^{II} ion of the ring is in this edge.[39] At the center of each ring is a [$^{n}Pr_2NH_2$]$^+$ cation, which H bonds to the fluoride ligands.

The resulting V-shaped, dimeric supramolecular assembly in **3a**–**3c** of crystallographic C_2 molecular symmetry shows an almost perpendicular orientation of the mean metal planes of the {Cr_7Ni} rings with respect to the mean metal plane of the central {Ru_2M} triangle (dihedral angles of 81.54(4)° [**3a**], 82.16(3)° [**3b**], and

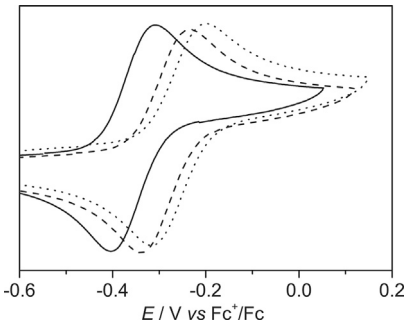

Figure 4. Cyclic Voltammograms of 2a–2c
2a (dotted line), **2b** (dashed line), and **2c** (solid line) in dichloromethane (0.1 M nBu$_4$PF$_6$, 25°C) with a scan rate of 100 mV s^{-1}.

81.30(3)° [**3c**]). The intramolecular metal-metal distances through the bridging *iso*-nicotinate ligands are 8.957(3) Å (**3a**), 8.947(4) Å (**3b**), and 8.924(6) Å (**3c**). The metrics of the two different component parts of each supramolecular assembly in **3a–3c** remain largely unchanged from those of the starting precursors **1**[9a] and **2a–2c** and have just subtle differences in the bond distances within the central triangular linking units as a result of the replacement of the terminal pyridine ligands in **2a–2c** by bridging *iso*-nicotinate ones in **3a–3c** (Table S1).

In the crystal lattice of **3a–3c**, the dimeric supramolecular assemblies are rather well separated from each other (Figure S8). The shortest intermolecular metal-metal distances between adjacent entities are 8.996(5) Å (**3a**), 9.015(4) Å (**3b**), and 8.996(3) Å (**3c**).

Electrochemical Properties

The cyclic voltammograms of **2a–2c** and the corresponding supramolecular dimeric assemblies **3a–3c** in dichloromethane (25°C, 0.1 M nBu$_4$NPF$_6$) are shown in Figures 4 and 5, respectively. A summary of the electrochemical data for **2a–2c** and **3a–3c** is given in Tables S4 and S5, respectively. The cyclic voltammograms of **2a–2c** and **3a–3c** at different scan rates are shown in Figure S9.

Mixed-Metal Triangular Clusters

2a–2c show a first reversible one-electron oxidation wave at E_1 = −0.22 V (**2a**), −0.24 V (**2b**), and −0.31 V (**2c**) versus Fc$^+$/Fc and show anodic to cathodic peak separation values (ΔE_1 = 80 mV) similar to that of the ferrocene/ferrocenium pair (ΔE_p[Fc$^+$/Fc] = 80 mV) under the same conditions (CH_2Cl_2, 0.1 M nBu$_4$NPF$_6$, 25°C). This oxidation is well separated from a second quasi-reversible one-electron oxidation wave at E_2 = +1.04 V (**2a**), +1.18 V (**2b**), and +0.79 V (**2c**) versus Fc$^+$/Fc (ΔE_2 = 87 mV) (Figure 4).

The almost equal values of E_1 for **2a** and **2b** indicate that the oxidation locus is the ruthenium(III) ion in both cases (given the unfeasible oxidation of the zinc(II) ion), as found earlier for the acetate homologs.[46–49] The lower E_1 value for **2c** suggests that the oxidation takes place on the cobalt(II) ion, which is in agreement with the crystallographic data (see above) as well as the magnetic and spectroscopic properties of **2c**^{ox} (see below). All three compounds also show a completely irreversible one-electron reduction wave at E_1 = −1.74 V (**2a**), −1.74 V (**2b**), and −1.89 V (**2c**) versus Fc$^+$/Fc (not shown).

Dimeric Ring Assemblies

Complexes **3a–3c** each undergo only one pseudoreversible one-electron oxidation wave at E_1 = −0.26 V (**3a**), −0.29 V (**3b**), and −0.35 V (**3c**) versus Fc$^+$/Fc (ΔE_1 = 87 mV) (Figure 5), together with an irreversible one-electron reduction wave at E_3 = −1.84 V (**3a**), −1.84 V (**3b**), and −1.87 V (**3c**) versus Fc$^+$/Fc (not shown). Once again, the fact

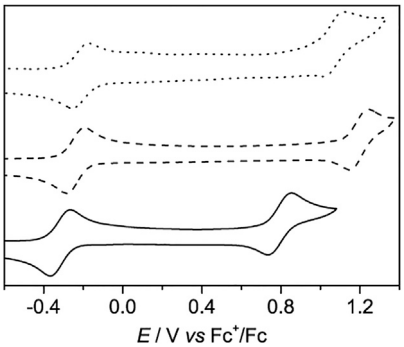

Figure 5. Cyclic Voltammograms of 3a–3c
3a (dotted line), **3b** (dashed line), and **3c** (solid line) in dichloromethane (0.1 M nBu$_4$PF$_6$, 25°C) with a scan rate of 100 mV s^{-1}.

that the values of E_1 are almost equal for **3a** and **3b**, and somewhat lower for **3c**, suggests that the oxidation locus is either Ru (**3a** and **3b**) or Co (**3c**), as for the parent precursors **2a–2c**.

Magnetic Properties

Mixed-Metal Triangular Clusters

The molar magnetic susceptibility ($\chi_M T$) of complexes **2a–2c** and the corresponding monooxidized species **2a^{ox}–2c^{ox}** was studied as a function of temperature (Figure S10). The magnetization M as a function of field H was measured at 2 and 4 K (Figures S12 and S13). All the data show that, for each redox pair, the magnetic properties can be switched by choice of oxidation state. The fits described below involve fitting both $\chi_M T(T)$ and $M(H)$ data.

The [Ru$^{III}_2$Zn^{II}] derivative **2a** was almost diamagnetic at room temperature and showed only a weak and linear $\chi_M T$ behavior consistent with a temperature-independent paramagnetism (TIP; Figure S10A). The diamagnetism is due to very strong antiferromagnetic coupling between the two low-spin Ru^{III} ions ($S_{Ru1} = S_{Ru2} = 1/2$), giving an $S = 0$ ground state for the triangle ($J \geq -1{,}000$ cm^{-1}). Modeling the weak linear $\chi_M T(T)$ for **2a** due to TIP gives $\chi_{TIP} = 1{,}580 \times 10^{-6}$ cm^3 mol^{-1}; this arises from the second-order Zeeman effect between the non-magnetic ground state and higher magnetic states.[51–53] The experimental susceptibility data for **2b** and **2c** were corrected with the TIP measured for **2a**.

For **2b**, the room-temperature $\chi_M T$ value of 1.22 cm^3 K mol^{-1} is close to that calculated for the spin-only value for an $S = 1$ state. $\chi_M T$ remained temperature independent to about 20 K and then decreased to 0.40 cm^3 K mol^{-1} at 2.0 K as a consequence of a non-negligible zero-field splitting (ZFS) (Figure S10B).

In **2b** and **2c**, the Ru^{III}-Ru^{III} coupling greatly exceeded that between each Ru^{III} and the high-spin 3d^8 Ni^{II} ($S_{Ni} = 1$) and 3d^7 Co^{II} ($S_{Co} = {}^3/_2$), producing $S = 1$ and $S = 3/2$ ground states, respectively. However, the magnetic properties in such triangles are not always explicable as being caused by the isolated divalent 3d ions. Recent studies[54] of the analogous [Ru$^{III}_2$Mn^{II}O(^{t}BuCO$_2$)$_6$(py)$_3$] cluster showed that a very large ZFS of the $S = 5/2$ ground state was caused by an interaction with Ru^{III} through antisymmetric exchange (ASE; also known as Dzyaloshinski-Moriya exchange).[55–60] A similar effect was operational here for the ZFS of the $S = 1$ state of **2b**.

The magnetic properties of **2b** were first fitted with a spin Hamiltonian (Equation 1) for an isolated $S = 1$, with axial (D) and rhombic (E) ZFS parameters, to give $g = 2.174$ and $|D| = 8.1$ cm^{-1} (with $E_{Ni} = 0$). This value was corroborated by high-frequency

EPR measurements (see below). High-frequency EPR studies of $[Fe^{III}_2Ni^{II}O(^tBuCO_2)_6(py)_3]$ gave D_{Ni} of -4.0 cm^{-1} (see Supplemental Information for more details), and therefore the very large ZFS parameter in **2b** is not exclusively caused by single-ion anisotropy of Ni^{II}.

$$\widehat{H}_{GS} = g\mu_B \widehat{S}\cdot H + D\left(\widehat{S}_z^2 - \frac{S(S+1)}{3}\right) + E\left(\widehat{S}_x^2 - \widehat{S}_y^2\right) \qquad \text{(Equation 1)}$$

The data were fitted with Equation 2, which includes ASE. Here, J_1 and J_2 are the magnetic coupling constants between the Ru^{III} ions and between the Ru^{III} ion and the high-spin Ni^{II} ion, respectively. Parameters $\mathbf{d_1}$ and $\mathbf{d_2}$ are the corresponding ASE vectors.[55–60]

$$\widehat{H} = -2J_1\left(\widehat{S}_{Ru1}\cdot\widehat{S}_{Ru2}\right) - 2J_2\left(\widehat{S}_{Ru1}\cdot\widehat{S}_{Ni} + \widehat{S}_{Ru2}\cdot\widehat{S}_{Ni}\right) + \mathbf{d}_1\cdot\left[\widehat{S}_{Ru1}\times\widehat{S}_{Ru2}\right] + \mathbf{d}_2\cdot\left[\widehat{S}_{Ru1}\times\widehat{S}_{Ni} + \widehat{S}_{Ni}\times\widehat{S}_{Ru2}\right] + D_{Ni}\left[\widehat{S}_{zNi}^2 - \frac{S_{Ni}(S_{Ni}+1)}{3}\right] \qquad \text{(Equation 2)}$$

Good fits of the experimental data of **2b** (solid line in Figure S10B) can be obtained for $J_1 = -1{,}000$ cm^{-1}, $J_2 = -100$ cm^{-1}, and $\mathbf{d}_2{}^z = 138.4$ cm^{-1} (with $\mathbf{d}_1{}^z = 0$). Note that these are indicative parameters because J_1 and J_2 are not known, but J_1/J_2 must be of this order.[54] The parameter D_{Ni} was fixed at -4.0 cm^{-1} from high-frequency and field EPR measurements on $[Fe^{III}_2Ni^{II}O(^tBuCO_2)_6(py)_3]$ (see Supplemental Information for more details).

The $\chi_M T(T)$ data for **2c** is typical for an octahedral, high-spin d^7 Co^{II} site ($^4T_{1g}$ term in ideal O_h symmetry) [61,62] and in agreement with the acetate analog previously reported.[48] The room-temperature $\chi_M T$ value was 3.03 cm^3 K mol^{-1}, well above the spin-only value for a spin quartet, and the decrease in $\chi_M T$ on cooling was caused by the spin-orbit coupling (SOC) effects (Figure S10C), giving a well-isolated ground Kramer spin-orbit doublet.

The least-squares fit of the experimental data of **2c** according to the Hamiltonian in Equation 3 [61](with a fictitious $L_{Co} = 1$ due to the T-P isomorphism) gave $\sigma = -1.26$, $\lambda_{Co} = -155.9$ cm^{-1}, and $\Delta = 239.9$ cm^{-1} (solid line in Figure S10C), where σ is the orbital reduction parameter, λ_{Co} is the SOC constant, and Δ is the axial distortion parameter. The orbital reduction parameter is defined as $\sigma = A\kappa$, where A varies between –3/2 (weak field) and -1 (strong field) and κ is the orbital reduction factor ($0 \leq \kappa \leq 1$). The values obtained from the fit are in agreement with literature values.[61,62]

$$\widehat{H} = \mu_B\left(\sigma\widehat{L}_{Co} + g_e\widehat{S}_{Co}\right)H + \lambda\left(\sigma\widehat{L}_{Co}\cdot\widehat{S}_{Co}\right) + \Delta\left[\widehat{L}_z^2 - \frac{1}{3}L(L+1)\right] \qquad \text{(Equation 3)}$$

The $\chi_M T(T)$ data for $\mathbf{2a^{ox}}$ show a linear decay with temperature to about 20 K, which is consistent with an isolated $S = 1/2$ with large TIP (Figure S10A).[51] There was then a more rapid decrease to 0.24 cm^3 K mol^{-1} at 2.0 K, which we assign to weak intermolecular interactions. The data for $\mathbf{2a^{ox}}$ were fit to the Curie-Weiss law together with TIP, and the best fit gave $g_{Ru} = 1.90$, TIP = 2,250 × 10^{-6} cm^3 mol^{-1}, and $\theta = -0.96$ K (Figure S10A). The very large TIP is due to the sizable TIP of the low-spin d^5 Ru^{III} ion and the even larger TIP of a low-spin d^4 Ru^{IV} site.[48,51–53] The observation is that $\mathbf{2a^{ox}}$ behaves as $S = 1/2$ at all temperatures, and hence, in the following analyses, we treat the $Ru^{III/IV}_2$ fragment as a single $S_{Ru2} = 1/2$ center because clearly Zn^{II} has a spin of 0.

The $\chi_M T(T)$ data for $\mathbf{2b^{ox}}$ show a $\chi_M T$ value of 0.45 cm^3 K mol^{-1} at 2 K, which corresponds to an $S = 1/2$ ground state resulting from an antiferromagnetic coupling

between the $Ru^{III/IV}{}_2$ (S_{Ru2} = 1/2) and Ni^{II} (S_{Ni} = 1) sites. Thermal population of the S = 3/2 excited state is responsible for the small increase in $\chi_M T$ with T, which reached a maximum $\chi_M T$ value of 1.27 cm^3 K mol^{-1} at room temperature. The least-squares fit of the experimental data for **2b^{ox}** according to Equation 4 gave J = −136 cm^{-1}, g_{Ru2} = 1.85, and g_{Ni} = 2.10, where J is the magnetic coupling parameter and g_{Ru2} and g_{Ni} are Landé factors.

$$\widehat{H} = -2J\left(\widehat{S}_{Ru2}\cdot\widehat{S}_{Ni}\right) + \mu_B\left(g_{Ru2}\widehat{S}_{Ru2} + g_{Ni}\widehat{S}_{Ni}\right)\cdot H \qquad \text{(Equation 4)}$$

The temperature dependence of $\chi_M T$ for **2c^{ox}** shows a linear decrease with temperature, as for **2a** and as expected for a [$Ru^{III}{}_2Co^{III}$] triangular unit with an S = 0 ground state due to the very strong antiferromagnetic coupling between the two low-spin Ru^{III} ions (S_{Ru1} = S_{Ru2} = 1/2). The residual susceptibility measured is due to TIP = 1,680 × 10^{-6} cm^3 mol^{-1} from the Ru^{III} atoms. This is very similar to the TIP measured for **2a**.

Dimeric Ring Assemblies

The magnetic properties of **3a–3c** and the corresponding oxidized species **3a^{ox}–3c^{ox}** in the form of both the $\chi_M T(T)$ and $M(H)$ plots are shown in Figure S11. In all cases, the $\chi_M T(T)$ and $M(H)$ data can be modeled as the sum of the components present. Therefore, the bulk magnetic measurements give little information on the exchange interactions between the {$Cr^{III}{}_7Ni^{II}$} rings and the $[Ru_2M]^n$ triangular links.

The $\chi_M T(T)$ plots for **3a–3c** and **3a^{ox}–3c^{ox}** are dominated by the {Cr_7Ni} rings, which have antiferromagnetic coupling between the seven Cr^{III} ions (S_{Cr} = 3/2) and one Ni^{II} ion (S_{Ni} = 1) (Figure S11). Only small differences were observed between each redox pair and were better seen in $M(H)$ measurements; the difference was most significant for the redox pair **3c**/**3c^{ox}** (Figure S11C).

X-Ray Absorption Spectra

To reveal the site of the metal oxidation in **2b^{ox}** and **2c^{ox}**, X-ray absorption near-edge structure (XANES) spectra were measured for the redox pairs **2b**/**2b^{ox}** and **2c**/**2c^{ox}** at the nickel and cobalt K-edges, respectively (Figure S15).

The Ni K-edge XANES spectra of both **2b** and **2b^{ox}** exhibited a very intense and symmetrically shaped edge band at 8,348.7 eV (**2b**) and 8,348.9 eV (**2b^{ox}**), which is characteristic of the 1s → 4p transitions in weakly distorted octahedral high-spin Ni^{II} complexes.[63] The spectra were practically superimposable, but **2b^{ox}** showed a minute shift to higher energy as a result of the additional overall charge upon oxidation.

The Co K-edge XANES spectrum of **2c** exhibited a very intense and symmetrically shaped edge band at 7,725.2 eV, corresponding to the 1s → 4p transitions, and there were no observable structures in the rising edge, as expected for weakly distorted octahedral high-spin Co^{II} complexes.[62] The spectrum of **2c^{ox}** presented a less intense and asymmetrically shaped edge band at 7,729.7 eV, typical of octahedral low-spin Co^{III} complexes.[62] The decrease in edge intensity for **2c^{ox}** could be due to the shorter metal-ligand distances characteristic of the low-spin Co^{III} ion, which enhance the metal-ligand mixture and ultimately lead to a weaker intensity for the corresponding 1s → 4p absorption.

The XANES spectra therefore support the electrochemical and structural data that suggest that the oxidation in **2b^{ox}** is ruthenium based but that in **2c^{ox}** is cobalt based.

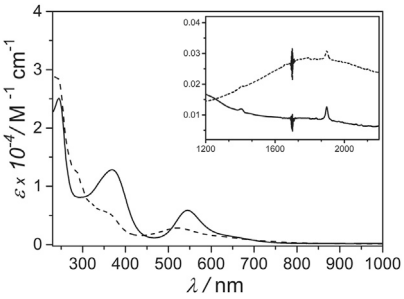

Figure 6. Electronic Spectra of 2a–2a^{ox}
2a (solid line) and **2a^{ox}** (dashed line) in dichloromethane at room temperature. The insets show the NIR region.

Electronic Absorption Spectra

The electronic absorption spectra of **2a–2c** and the corresponding oxidized species **2a^{ox}–2c^{ox}** are compared in Figures 6 and S16. The electronic absorption spectra for **2a–2c** show a common pattern, including two well-resolved intense peaks in the high- and low-energy UV regions and a peak of lower intensity in the visible zone with a distinct shoulder in the low-energy tail (Table 2). By resemblance with the spectra of related oxo/carboxylato-bridged diruthenium(III) complexes, the visible band can be assigned to a transition between mixed, ground, and excited states composed of combinations of Ru dπ and O pπ orbitals of the Ru–O–Ru subunit.[42,43,46,64–67]

The electronic absorption spectra of the oxidized species **2a^{ox}–2c^{ox}** showed an intense, more or less resolved peak in the high-energy UV region and two distinct shoulders extending into the low-energy UV region, together with a peak of lower intensity in the visible region and several shoulders in either the low-energy (**2a^{ox}** and **2b^{ox}**) or high-energy (**2c^{ox}**) sides (Table 2).

A modest blue shift was observed for the visible band of **2a^{ox}–2c^{ox}** in comparison with **2a–2c**, which was accompanied by a noticeable increase in their intensity for **2c^{ox}**. In addition, a new band of weak intensity appeared in the near infrared (NIR) region (inset of Figures 6 and S16 and Table 2). This weak NIR band can be attributed to an intervalence charge transfer (IVCT) transition between the low-spin Ru^{III} and Ru^{IV} ions in **2a^{ox}** and **2b^{ox}** or between the low-spin Ru^{III} and Co^{III} ions in **2c^{ox}**. Although a low-energy band (λ_{max} = 1,190 nm) of similar intensity was recently found in mixed-valent Ru^{III}–O–Ru^{IV} complexes of class III,[68] we are unaware of any previous reported charge-transfer band in mixed-metal Ru^{III}–O–Co^{III} complexes.

EPR Spectra

Mixed-Metal Triangular Clusters

Continuous-wave EPR measurements in the X- (ca. 9.5 GHz), K- (ca. 24 GHz), Q- (ca. 34 GHz), and W-(ca. 94 GHz) bands were performed for **2a–2c** and the corresponding monooxidized species **2a^{ox}–2c^{ox}** at low temperature.

2a gave no EPR signal because of its diamagnetic singlet ground state, which is the only populated state even at room temperature (see Magnetic Properties), contrary to the spectrum recorded by Kobayashi et al.[47] on a polycrystalline sample of the Ru_2Zn acetate analog, which conceivably stems from a mononuclear Ru^{III} impurity based on the reported *g* values.

Because of the large ZFS of the *S* = 1 ground state of **2b** (see Magnetic Properties), an EPR spectrum could be seen only at high frequency (331.2 GHz). This contrasts with

Table 2. Selected UV/Visible-NIR Spectroscopic Data in Dichloromethane at 25°C for 2a–2c and $2a^{ox}$–$2b^{ox}$

Compound	λ_1 (nm)[a]	λ_2 (nm)[a]	λ_3 (nm)[a]	λ_4 (nm)[a]
2a	245 (2.51)	369 (1.28)	544 (0.59), 636sh	–
2b	248 (2.57)	382 (1.37)	561 (0.78), 669sh	–
2c	246 (2.46)	382 (1.19)	566 (0.62), 645sh	–
$2a^{ox}$	256 (2.59), 292sh, 357sh	–	518 (0.28), 634sh	1,786 (0.03)
$2b^{ox}$	259 (2.65), 295sh, 358sh	–	529 (0.73), 586sh, 739sh	1,720 (0.04)
$2c^{ox}$	239 (5.59), 294sh, 329 sh	–	543 (1.42), 490sh	1,678 (0.02)

[a]The values of the molar extinction coefficient ($\varepsilon \times 10^{-4}/M^{-1}\ cm^{-1}$) are given in parentheses.

the reported X-band spectrum for a polycrystalline sample of the Ru_2Ni acetate analog,[48] which we surmise, given the reported g values, arises from either a mononuclear Ru^{III} impurity or trace amounts of trinuclear $[Ru^{III}{}_3O]^+$ species.[51] The high-frequency EPR spectra of polycrystalline **2b** at 5 K showed multiple lines at resonant fields of ca. 2,500 mT (Figure 7). These are due to magnetically distinct but similar species arising from the arrangement of the molecules in the solid state and/or the presence of crystallographically distinct molecules within the asymmetric unit, but with D ca. 8 cm^{-1} in each case. Given that high-frequency EPR spectra of the $Fe^{III}{}_2Ni$ analog give D_{Ni} = 4.0 cm^{-1}, the large $D \approx 8.0\ cm^{-1}$ for **2b** must arise from an ASE interaction,[54] and accordingly, the EPR spectrum of **2b** was simulated with Equation 2. Satisfactory simulations were obtained with the J and $\mathbf{d}_i^z$ values used for fitting the magnetic data (see above), g_{Ni} = 2.20, g_{Ru} = 2.00, and three sets of ZFS parameters (see Supplemental Information for more details): $D_{Ni} = -2.7$, -3.5, or $-4.25\ cm^{-1}$. The spectral intensity was mapped by weighting the subspectra in a ratio of 1.4:2.2:1 (Figures 7 and S18). The values for g and D agree with the magnetic susceptibility data.

The Q-band EPR spectra of frozen dichloromethane/toluene solutions of **2c** at 10 K are typical of a high-spin Co^{II} ion with unquenched orbital angular momentum (Figures 8 and S19). These spectra were simulated as a S_{eff} = 1/2 (see Magnetic Properties), giving rhombic effective g values of g_1 = 5.61, g_2 = 4.05, and g_3 = 2.77, which are similar to those found for the acetate analog.[48] The average g value of 4.14 is comparable with the calculated value of 4.17 for the J = 1/2 ground state in the fitting of the magnetic data. The coupling of the electron spin to the I = 7/2 nuclear spin of ^{59}Co (100% natural abundance) was evident on g_1 and g_2 at the X band. Simulation of this spectrum gave A_1 = 180, A_2 = 138, and $A_3 = 20 \times 10^{-4}\ cm^{-1}$.

Polycrystalline samples of **2c** showed two distinct but similar species, which were better resolved at higher frequencies: the W-band spectrum exhibited additional lines at g_1 and g_3, which were even more apparent at high-frequency and field EPR measurements (331.2 GHz; Figure S20). The spectra were simulated with two sets of g values with equal weighting: g_1 = 6.377, g_2 = 4.247, and g_3 = 2.888 and g_1 = 5.354, g_2 = 4.247, and g_3 = 2.640. This is a solid-state effect because only one species was observed in the solution spectra (Figure 8).

Compounds $\mathbf{2a^{ox}}$–$\mathbf{2c^{ox}}$ were prepared in situ from the 1:1 stoichiometric oxidation of **2a–2c** with a 3 mM dichloromethane/toluene solution of $[FeCp_2](PF_6)$. The X-band EPR spectrum of frozen dichloromethane/toluene solutions of $\mathbf{2a^{ox}}$ at 30 K was consistent with the large g anisotropy of an S_{Ru2} = 1/2 on the mixed-valent diruthenium(III,IV) moiety of $[Ru_2{}^{III/IV}Zn^{II}]$ (Figure 9A). Simulation gave g_1 = 2.414, g_2 = 1.758, and g_3 = 1.381, which are similar to the values found for the related

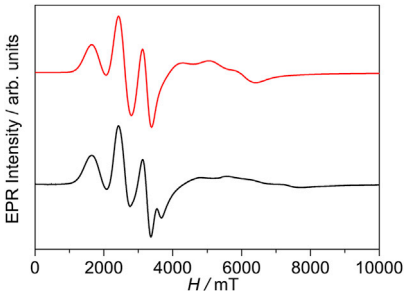

Figure 7. Powder High-Frequency and Field EPR Spectra of 2b at 5 K

Experimental (black trace) and simulated (red trace). The simulation included accounting for the ASE effects (see text).

mixed-valent diruthenium(III,IV) complexes of formula $[Ru_2O(RCO_2)L_6]^{3+}$ (R = Me, C_6H_4-*p*-OMe, C_6H_4-*p*-Me; L = imidazole) reported by Sudha et al.[67] The average *g* value of 1.85 was comparable with that calculated from the fitting of the magnetic data of **2a**^{ox} (see Magnetic Properties).

The Q- and X-band spectra of frozen dichloromethane/toluene solutions of **2b**^{ox} at 30 K (Figures 9B and S21, respectively) were characteristic of an axial spin doublet ground state ($g_\perp > g_{||}$), which arises from the antiferromagnetic exchange between the Ni^{II} and $Ru^{III/IV}{}_2$ sites. The perpendicular *g* components were resolved at the Q band. The experimental data could be simulated with $g_1 = 2.339$, $g_2 = 2.306$, and $g_3 = 2.034$. These *g* values are consistent with arising from antiferromagnetic coupling and the projection of the $Ru_2^{III/IV}$ (from **2a**^{ox}) and Ni *g* values (2.2) on the $S = 1/2$ ground state ($g = 4g_{Ru2}/3 - g_{Ni}/3$).

Compound **2c**^{ox} was found to be EPR silent, as expected for an $[Ru^{III}{}_2Co^{III}]$ triangular unit with an $S = 0$ ground state.

Dimeric Ring Assemblies

The magnetic interactions between the $\{Cr_7Ni\}$ rings and the central triangles in **3** and **3**^{ox} were too weak for measurement by magnetometry, so we probed these interactions by EPR, which is much more sensitive to very weak exchange interactions. Because the central triangle is heterometallic, each sample contains two linkage isomers: one where both rings are attached to Ru centers and one where one ring is attached to an Ru and one is attached to the divalent 3d metal.

3a^{ox}–**3c**^{ox} were prepared in situ from the 1:1 stoichiometric oxidation of **3a**–**3c** with a 3 mM dichloromethane/toluene solution of $[FeCp_2](PF_6)$, and the reversibility of the redox processes was confirmed by subsequent 1:1 stoichiometric reduction with a 3 mM dichloromethane/toluene solution of $[CoCp_2]$, which regenerated the EPR spectra of **3a**–**3c** (Figures 10, 11, and 12).

The K-band EPR spectrum of **3a** at 5 K in CH_2Cl_2/toluene was very simple in that it comprised just the $S = 1/2$ spectrum of magnetically isolated $\{Cr_7Ni\}$ rings[69] with $g_x = g_y = 1.78$ and $g_z = 1.74$ (Figure 10). Upon oxidation of **3a**, more resonances were observed because the linking $Ru_2^{III/IV}Zn^{II}$ triangle was paramagnetic. The spectrum of **3a**^{ox} was not simply the summation of that of **2a**^{ox} and $\{Cr_7Ni\}$ given that it showed a prominent feature at ca. 850 mT. However, there are very few additional features to be simulated. Our best simple model involved an isotropic interaction between the $S = 1/2$ $[Ru^{III,IV}{}_2Zn^{II}]$ triangle (S_1) and only one of the two $S = 1/2$ $\{Cr_7Ni\}$ rings (S_3)—Hamiltonian Equation 5—to give an estimate of $J = -0.2$ cm^{-1} with known *g* tensors. This implies that the second $\{Cr_7Ni\}$ ring is uncoupled, and the model corresponds to a linkage isomer where one ring is attached to an Ru

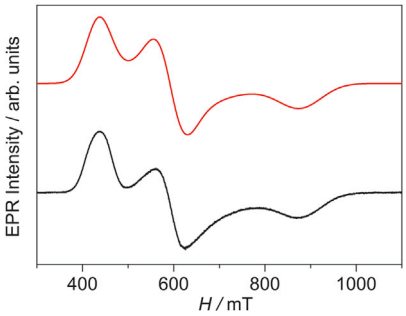

Figure 8. Q-Band EPR Spectra of Frozen Solutions of 2c

Frozen-matrix dichloromethane/toluene solutions of **2c** (black trace) compared with the simulated spectra (red trace). Simulation parameters are given in the text.

site and the second is attached to Zn. A better simulation might be possible by inclusion of the second linkage isomer, but the data do not justify additional parameters. Reduction of $\mathbf{3a}^{ox}$ back to **3a** regenerates the original spectrum.

$$\widehat{H} = -2J\left(\widehat{S}_1 \cdot \widehat{S}_2\right) + \mu_B\left(\widehat{S}_1 \cdot \underline{g}_1 + \widehat{S}_2 \cdot \underline{g}_2 + \widehat{S}_3 \cdot \underline{g}_3\right) \cdot H \qquad \text{(Equation 5)}$$

These spectra, where the coupling of the two $\{Cr_7Ni\}$ units to the linking triangle is asymmetric, would mean that the **3a** and $\mathbf{3a}^{ox}$ are not suitable for the √iSWAP gate.

The K-band EPR spectrum of frozen dichloromethane/toluene solutions of **3b** at 5 K can be simulated with Hamiltonian Equation 6, which invokes an isotropic exchange between the $[Ru^{III}_2Ni^{II}]$ triangle (S_2) and the two $S = 1/2$ $\{Cr_7Ni\}$ rings (S_1 and S_3) with known ZFS and g parameters, giving $J = -0.024\ cm^{-1}$.

$$\widehat{H} = -2J\left(\widehat{S}_1 \cdot \widehat{S}_2 + \widehat{S}_2 \cdot \widehat{S}_3\right) + D_2\left[\widehat{S}^2_{z2} - \frac{S_2(S_2+1)}{3}\right] + E_2\left(\widehat{S}^2_{x2} - \widehat{S}^2_{y2}\right) + \mu_B\left(\widehat{S}_1 \cdot \underline{g}_1 + \widehat{S}_2 \cdot \underline{g}_2 + \widehat{S}_3 \cdot \underline{g}_3\right) \cdot H \qquad \text{(Equation 6)}$$

The EPR spectrum of $\mathbf{3b}^{ox}$, where the central node is now $S = 1/2$ is much more complicated; efforts to simulate this (Hamiltonian Equation 7 with known g values) gave a best estimate of $J = -0.04\ cm^{-1}$. The simulation is not perfect; an unambiguous understanding of this spectrum would require a single-crystal study. Reduction of $\mathbf{3b}^{ox}$ back to **3b** regenerates the original spectrum.

$$\widehat{H} = -2J\left(\widehat{S}_1 \cdot \widehat{S}_2 + \widehat{S}_2 \cdot \widehat{S}_3\right) + \mu_B\left(\widehat{S}_1 \cdot \underline{g}_1 + \widehat{S}_2 \cdot \underline{g}_2 + \widehat{S}_3 \cdot \underline{g}_3\right) \cdot H \qquad \text{(Equation 7)}$$

EPR spectra of **3c** under the same conditions were much better resolved (Figure 12) and clearly showed exchange between the two $S = 1/2$ $\{Cr_7Ni\}$ rings and the $S_{eff} = 1/2$ $\{Ru_2Co\}$ central node. The exchange was smaller than their difference in Zeeman energy ($\mu_B \Delta g_{Ring-C.node} H \gg |J|$), giving an AX_2 spin pattern with the $\{Cr_7Ni\}$ ring (the X spins) split into a doublet. $\{Ru_2Co\}$ resonances (the A spin) should split into a 1:2:1 triplet; this is unresolved (Figure 12).[70] Nevertheless, the exchange interaction between the spins, J, can be read directly from the $\{Cr_7Ni\}$ ring doublet splitting. This, and simulations with Hamiltonian Equation 7 (with fixed known g values), gives $J = -0.026\ cm^{-1}$ (Figure 12). Complex $\mathbf{3c}^{ox}$ gives EPR spectra for an isolated $\{Cr_7Ni\}$ ring. Reduction of $\mathbf{3c}^{ox}$ back to **3c** regenerates the original spectrum.

Because the exchange in **3c** is symmetric (Hamiltonian Equation 7) and $\mathbf{3c}^{ox}$ only contains the isolated qubit, this redox pair is promising for implementing the √iSWAP gate. Therefore, we measured T_1 and T_M for both complexes of the redox pair.

For **3c** and $\mathbf{3c}^{ox}$, we found T_1 of about 24 μs at 2.7 K (see Table S6), 3–4 orders of magnitude longer than our elementary gates. For resonances assigned to the

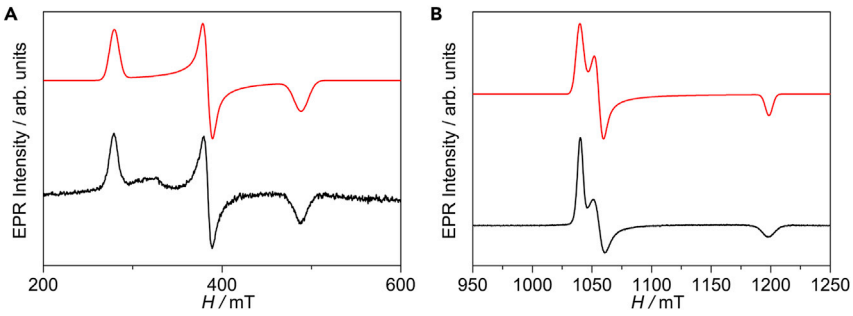

Figure 9. EPR Spectra of Frozen Solutions of $2a^{ox}$ and $2b^{ox}$

Experimental (black trace) and simulated (red trace) spectra of frozen-matrix dichloromethane/toluene solutions of $\mathbf{2a}^{ox}$ (X-band, A) and $\mathbf{2b}^{ox}$ (Q-band, B) at 30 K, respectively.

{Cr_7Ni} rings, we found T_M = 749 and 767 ns for **3c** and $\mathbf{3c}^{ox}$, respectively, for 0.0001 M solutions in toluene (Table 3), demonstrating that the phase memory times are not strongly influenced by magnetic interactions with the central node. To measure T_M for resonances associated with the {Ru_2Co^{II}} unit in **3c**, we had to use a 0.002 M solution, and here we found that T_M varied from 245 to 706 ns depending on the resonance studied. These results are used in the simulations below, where we show that the measured phase memory times are sufficiently long (Tables 3 and S6–S8 and Figures 13 and S24–S29) for implementing complex sequences of gates.

QIP with Compound 3c

In this section, we describe a scheme for implementing single- and two-qubit gates on the dimeric ring assembly **3c**, i.e., where there is the same coupling between each of the two qubits and the bridging node when the bridging node is paramagnetic. These are the elementary steps of quantum computation and quantum simulation algorithms. The scheme[71] exploits the reversible redox properties of the central node in **3c**. These can be exploited to implement a √iSWAP two-qubit gate on the {Cr_7Ni} qubits, whose effect on the computational basis is

$$|00\rangle \rightarrow |00\rangle$$
$$|01\rangle \rightarrow \frac{|01\rangle + i|10\rangle}{\sqrt{2}}$$
$$|10\rangle \rightarrow \frac{|10\rangle + i|01\rangle}{\sqrt{2}}$$
$$|11\rangle \rightarrow |11\rangle \ .$$

Here, the logical states $|0\rangle$ and $|1\rangle$ are associated with the orientations $|\downarrow\rangle$ and $|\uparrow\rangle$, respectively, of the spin of each molecular qubit.

A first theoretical proposal was put forward by Lehmann et al.[9] They proposed using a polyoxometallate made up of a Keggin unit, $PMo_{12}O_{40}$, capped with two localized VO^{2+} centers with S = 1/2. The core acts as an electron reservoir and switches on or off the interaction between vanadyl units acting as qubits. This implements a √SWAP gate (equivalent to the √iSWAP in building efficient quantum circuits; see Supplemental Information and Fei et al.[72]) for particular sets of parameters of the trimer (qubit + switch in the "on" state) Hamiltonian. Indeed, for this gate to perform well, very specific ratios are required between the qubit-qubit exchange and the qubit-redox unit exchange. We present here a more flexible scheme for the √iSWAP gate, which relies not on a precise choice of the spin Hamiltonian parameters but

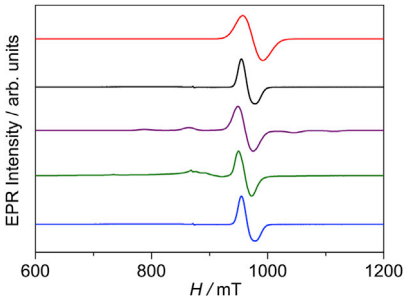

Figure 10. EPR Spectroscopy of 3a

Evolution of the K-band EPR spectra of frozen solutions of **3a** (black trace) after stoichiometric oxidation (green trace) and subsequent reduction (blue trace). The simulated spectra of **3a** (red trace) and **3a^{ox}** (purple trace) were obtained with the appropriate Hamiltonian (see text).

rather on the hierarchy of the involved interactions. As specified below, we only require that the rings have the same Zeeman energies and that ring-switch coupling is sufficiently smaller than the difference in Zeeman energies between the qubits and the switch.

A single electron can be injected or removed very quickly (picoseconds) with an STM tip at an appropriate potential, thus bringing the central switch from a magnetic (reduced, switched "on") to a diamagnetic (oxidized, switched "off") state.[5,9] Since the timescale of the electron-hopping process is orders of magnitude faster than our gates (some nanoseconds, see below), we can safely assume that the hopping occurs instantly. Hence, the hopping only influences the switch component of the wave function, which remains factorized from the state of the qubits. Such large tunneling rates guarantee that operations are not affected by the incoherent nature of the tunneling process, as already demonstrated by Lehmann et al.[9] with detailed numerical calculations.

The oxidation of the central node to its diamagnetic counterpart decouples the two qubits, thus allowing us to implement single-qubit operations with very high fidelity. This can be done by means of magnetic pulses applied along a direction perpendicular to the static field. For the simulations described below, we used an oscillating field with Gaussian envelope: $B_x(t) = B_0 e^{-(t-t_0)^2/2\sigma^2} \cos(\omega(t - t_0) + \phi)$. The frequency ω is chosen to match the Zeeman energy gap for the $M = -1/2$ (logical $|0\rangle$) $\rightarrow$ $M = 1/2$ (logical $|1\rangle$) transition of the {Cr_7Ni} qubits, whereas the phase ϕ controls the rotation axis in the xy plane of the Bloch sphere, and the pulse duration σ determines the rotation angle. Hence, we can obtain arbitrary single-qubit R_x and R_y rotations.

Conversely, when the switch is in the paramagnetic state (i.e., Ru_2Co^{II}), the system behaves as a trimer, described by Hamiltonian Equation 7, where the switch mediates an effective interaction between the qubits. The scheme[71] works if the two qubits are symmetrically coupled to the switch and have the same Zeeman energy but one different to that of the switch in the "on" state. This is the case in **3c**, where the g tensors of the qubits and switch are very different, i.e., g_z = 1.74 for {Cr_7Ni} rings and g_z = 2.77 for the central effective spin 1/2 triangular unit. Therefore, the ring-switch exchange J is smaller than the difference between the Zeeman energies of the switch and of the {Cr_7Ni} rings. Hence, the spin state of the switch is nearly frozen in the $M_s = -1/2$ state and has only small fluctuations induced by the switch-ring exchange interaction. For this reason, switch degrees of freedom can be eliminated, and this leads to an effective interaction between the two {Cr_7Ni} qubits, given by

$$\hat{H}_{qq} = \Gamma\left(\hat{S}_{x1}\hat{S}_{x2} + \hat{S}_{y1}\hat{S}_{y2}\right) + \lambda\left(\hat{S}_{z1} + \hat{S}_{z2}\right) \ , \qquad \text{(Equation 8)}$$

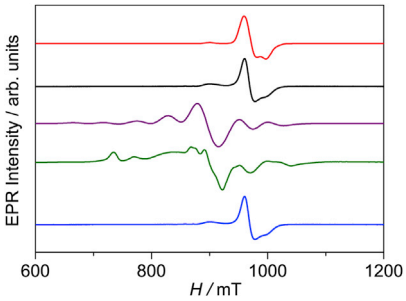

Figure 11. EPR Spectroscopy of 3b
Evolution of the K-band EPR spectra of frozen solutions of **3b** (black trace) after stoichiometric oxidation (green trace) and subsequent reduction (blue trace). The simulated spectra of **3b** (red trace) and **3b**^{ox} (purple trace) were obtained with the appropriate Hamiltonian (see text).

where the field is along z, $S_{1\alpha}$ and $S_{2\alpha}$ are the components of the first and second {Cr_7Ni} spins, respectively, along the α axis ($\alpha = x, y, z$), and

$$\Gamma = \frac{2\ J^2}{B\ \mu_B(g_{1z} - g_{Coz})}, \quad \lambda = J + \frac{J^2}{B\mu_B\ (g_{1z} - g_{Coz})}\ . \qquad \text{(Equation 9)}$$

Hamiltonian Equation 8 has been derived by eliminating the switch degrees of freedom at a second-order perturbation theory level (see Supplemental Information for a detailed derivation). It represents an effective qubit-qubit coupling that acts only when the switch is in its "on" state. For specific times ($\approx \pi/2\Gamma$), the evolution induced by Hamiltonian Equation 8 coincides with the $\sqrt{}$iSWAP gate, apart from single-qubit rotations along z due to the second term in Equation 8. These can be compensated by properly combining R_x and R_y single-qubit rotations, thanks to the decomposition $R_z(\varphi) = R_x(\pi/2)R_y(\varphi)R_x(-\pi/2)$.

To gain more insight into the feasibility of $\sqrt{}$iSWAP, we performed detailed calculations for compound **3c** by using a master equation formalism including the effect of pure dephasing due to the finite value of T_M (see Supplemental Information for details). As stated above, in the present assemblies, the effect of T_1 is completely negligible because it acts on a timescale much longer than our gates. Figure 14A shows a color map of the simulated fidelity of an $\sqrt{}$iSWAP gate as a function of the phase memory time of the rings (T_M^{ring}) and of the central switch triangle (T_M^{tr}). The two qubits are initialized on a random state with a static field of 3 T. The fidelity is defined by $F = \sqrt{\psi_T|\rho|\psi_T}$, where $|\psi_T\rangle$ is the target state after an ideal gate, whereas ρ is the actual final system density matrix. F is a measure of the proximity between the ideal, desired evolution (represented by $|\psi_T\rangle$), and the actual result of the implementation of the gates (ρ). In particular, F = 1 corresponds to an ideal implementation of the gates. By analyzing Figure 14A, we note that the dependence on T_M^{ring} is much more pronounced. Conversely, F is nearly independent of T_M^{tr}, even for T_M^{tr} values lower than the gate duration (approximately 4 ns). This is due to the fact that only virtual excitations of the switch are exploited for an effective qubit-qubit interaction, which represents a remarkable advantage of the present scheme. We also note that for the measured values of T_M^{ring}, the fidelity of the single gate is very high (above 99.3%).

These encouraging results allow us to consider a sequence of gates in order to obtain the quantum simulation of interesting physical models. A quantum simulator is a "quantum machine that can imitate other quantum systems."[1] In the present implementation, this machine is constituted by a pulsed EPR setup containing interacting Cr_7Ni qubits (the physical hardware), and the quantum system to be mimicked is our target. The quantum simulation can be obtained by mapping the target system onto the hardware and then decomposing the target time evolution into a sequence of elementary gates. As a result, the physical hardware mimics the time evolution of the target, whose properties can thus be extracted by the experimenter (see Aromí et al.[17] for more details). As a possible

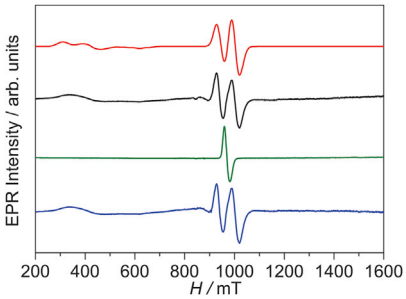

Figure 12. EPR Spectroscopy of 3c
Evolution of the K-band EPR spectra of frozen solutions of **3c** (black trace) after stoichiometric oxidation (green trace) and subsequent reduction (blue trace). The simulated spectrum of **3c** (red trace) was obtained with the appropriate Hamiltonian (see text).

proof-of-principle experiment, we consider here the simulation of the time evolution induced by the Heisenberg Hamiltonian in a magnetic field β:

$$H = \xi \mathbf{S}_1 \cdot \mathbf{S}_2 + \beta(S_{1x} + S_{2x}) \quad . \qquad \text{(Equation 10)}$$

The sequence of required operations is schematically shown in Figure 14B. The Heisenberg Hamiltonian can be decomposed as $H = \xi(S_{1x}S_{2x} + S_{1y}S_{2y} + S_{1z}S_{2z}) = \frac{\xi}{2}(H_{XY} + H_{XZ} + H_{YZ})$, where $H_{\alpha\beta} = S_{1\alpha}S_{2\alpha} + S_{1\beta}S_{2\beta} \quad (\alpha, \beta = x, y, z)$. Then, the three blocks (dashed boxes in Figure 14B) are obtained by combining free evolution intervals induced by H_{qq} (Equation 8) with proper rotations, as proposed in Las Heras et al.[73] Results are shown in Figure 14C), where we report the calculated time evolution of the total magnetization $S_z = S_{1z} + S_{2z}$ of the two qubits, initialized in a state in which the two qubits are parallel. We note that the calculated evolution (points) shows very good agreement with the expected oscillation (continuous line). Remarkably, the oscillation is well reproduced, not only in ideal conditions (blue points, no decoherence) but also with the inclusion of the T_M values measured by pulsed-EPR (red points).

Even if the performance of the setup in the implementation of the elementary gate had already been demonstrated,[71] the simulation of complex algorithms, involving many gates, is far from trivial. Indeed, this requires quantitative testing of the complex sequences of gates to show that they are robust with respect to errors due to decoherence or to the imperfect implementation of the gates. Here, we have numerically solved the density matrix master equation for the hardware spin Hamiltonian with the inclusion of the main decoherence processes. This allows us to directly show the feasibility of the proposed digital simulations. This is a significant step beyond our previous report of structures able to implement QGs, where we did not carry out such detailed simulations of the fidelity of operations.[71]

On the experimental side, the realization of the proposed scheme requires embedding an STM tip inside a pulsed-EPR spectrometer, which is to date the most important hurdle. Indeed, although several transport measurements have been performed on molecules arranged in a spintronics setup,[74,75] combining this with microwave pulses is a challenging task. In addition, individual molecules should be grafted on a metallic surface. This has already been demonstrated for $\{Cr_7Ni\}$ wheels[76] without altering the magnetic properties.

Conclusions

In summary, we report a family of oxo-centered mixed-metal $[Ru^{III}_2M]$ triangular clusters (M = Zn, Ni, and Co) and their use as redox-active linkers between two molecular qubits represented by pyridine-functionalized $\{Cr_7Ni\}$ rings for building supramolecular assemblies with potential application in the physical implementation of QIP. The scheme proposed requires the equivalent couplings between each of the two qubits

Table 3. Q-Band Pulsed-EPR Data for 3c and $3c^{ox}$

Compound	*B* (mT)	*T* (K)	T_M (ns)	*s*
3c	1,389	2.7	749 ± 1	1.696 ± 0.003[a]
$3c^{ox}$	1,374	2.5	767 ± 1	1.665 ± 0.003[a]
3c[b]	557 (▲)	2.6	666 ± 2	1
	557 (▲)	3.0	499 ± 2	1
	557 (▲)	3.3	439 ± 1	1
	557 (▲)	5.0	245 ± 5	1
	776 (■)	2.6	706 ± 3	1
	1,260 (◆)	2.6	693 ± 3	1.655 ± 0.014
	1,350 (●)	2.6	683 ± 5	1.568 ± 0.033

T_M represents the phase memory time, and *s* is a stretching parameter.

[a]Measurements performed in 0.0001 M toluene solutions at the maximum resonance field for the ring in each compound.

[b]Measurements performed in 0.002 M toluene solutions at the maximum resonance field for the ring in each compound.

The triangles, square, diamond, and circle refer to field positions where coherence times were measured (see Figure 13).

and the central link. This was observed by EPR spectra for the case where the central cluster is $\{Ru^{III}_2Co^{II}\}$ **3c** but not when it is $\{Ru^{III/IV}_2Zn^{II}\}$ $\mathbf{3a^{ox}}$. Crystallography suggests that, in both cases, Ru and M are disordered, and in one linkage isomer, the links would certainly be inequivalent. Our present thought is that, in **3c**, the unpaired electron is somewhat more delocalized than in $\mathbf{3a^{ox}}$, where the Zn^{II} site is always completely diamagnetic.

The performance of the proposed architecture was confirmed by extensive numerical simulations, which were based on experimental parameters and included the qubit pure dephasing in a master equation treatment. This suggests that **3c** is a promising candidate for proof-of-principle experiments involving the implementation of complex sequences of gates. In fact, it could constitute the basic building block of a scalable architecture, which could be used to simulate interesting physical models, and current efforts of our investigations are devoted to this direction.

In contrast with other proposals for QIP with molecular nanomagnets, which use global magnetic pulses to manipulate the state of an ensemble of equivalent molecules, here we propose using an STM tip for local control of the qubit-qubit interaction on an individual supramolecular dimer. Although experimentally challenging, the realization of this architecture, with local control of the qubit-qubit coupling at the molecular level, could greatly increase the class of solvable problems.

EXPERIMENTAL PROCEDURES

Materials

$[^nPr_2NH_2][Cr_7NiF_8(O_2C^tBu)_{16}]$ was synthesized according to methods documented in the literature[39] but $[2NiCO_3{\cdot}3Ni(OH)_2{\cdot}4H_2O]$ was used as the source of Ni(II) instead of the compound $[Ni_2(\mu\text{-}OH_2)(O_2C^tBu)_4(HO_2C^tBu)_4]$, and the reaction time was 24 hr at 160°C. A functionalized ring with *iso*-nicotinic acid $[^nPr_2NH_2][Cr_7NiF_8(O_2C^tBu)_{15}(O_2C\text{-py})]$ **1**, abbreviated as $\{Cr_7Ni\text{-}O_2C\text{-py}\}$, was obtained according to the reported procedure.[37] All chemicals were of reagent-grade quality, and they were purchased from commercial sources and used as received.

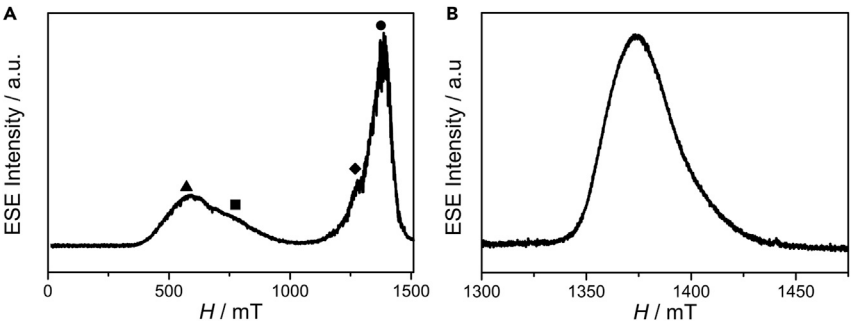

Figure 13. Q-Band Pulsed-EPR Spectroscopy for 3c and $3c^{ox}$

Echo-detected field-swept EPR spectra at Q-band for (A) **3c** and (B) $\mathbf{3c}^{ox}$ in 0.002 M (**3c**) or 0.0001 M ($\mathbf{3c}^{ox}$) toluene solutions. The triangle, square, diamond, and circle refer to field positions where coherence times were measured.

Physical Techniques

Nuclear magnetic resonance spectra were recorded on a Bruker AV 400 instrument. Chemical shifts are reported in parts per million (ppm) from low to high frequency and referenced to the residual solvent resonance. Electrospray ionization mass spectrometry and microanalysis were carried out by the services at the University of Manchester.

Preparation of $[Ru_2MO(O_2C^tBu)_6(py)_3]$: M = Zn 2a, Ni 2b, and Co 2c

A mixture of $RuCl_3$ (0.15 g, 0.57 mmol) and pivalic acid (22.1 g, 219 mmol) in 4:1 EtOH/H_2O (25 mL) was heated for 10 min at 70°C. After cooling to room temperature, $[Zn(O_2C^tBu)_2]$[44] (0.54 g, 2.01 mmol) or $[M_2(\mu\text{-}OH_2)(O_2C^tBu)_4(HO_2C^tBu)_4]$[45] (M = Ni or Co) (0.95 g, 2.01 mmol) was added, and the reaction mixture was stirred until all had dissolved and the color changed from red to purple. The solution was left to stand overnight and then filtered. The solvent was removed by rotary evaporation, and the resultant oil was filtered for removal of excess metal pivalate, treated with MeCN (10 mL), and then placed in the freezer (−40°C) overnight. Repeated freeze-filter cycles ensured the removal of excess pivalic acid. The solvent was then stripped under vacuum before distilled water (200 mL) was added to the purple residue, and the solution was stirred for 30 min. The solution was filtered to yield a dark purple solid, which was washed with 4:1 H_2O/MeCN (3 × 10 mL) and dried in air. The desired complex was obtained by dissolving 100 mg of the purple solid in MeCN (30 mL) and pyridine (10 mL) and then stirring the solution overnight and filtering. The solvent was removed by rotary evaporation, and X-ray quality crystals were obtained from recrystallization from pyridine.

Preparation of $[Ru_2MO(O_2C^tBu)_6(py)_3]PF_6$: M = Zn $2a^{ox}$, Ni $2b^{ox}$, and Co $2c^{ox}$

Under an N_2 atmosphere, a dark-purple solution of **2a**/**2b**/**2c** (0.100 g, 0.09 mmol) in CH_2Cl_2 (20 mL) was combined with $[FeCp_2](PF_6)$ (0.03 g, 0.09 mmol) and stirred for 30 min. The deep-purple solution was left to stand for 10 min before being filtered. Hexane (20 mL) was added, and the solution was concentrated to a third of the volume and placed in the freezer (−40°C) to crystallize. Unfortunately, only X-ray quality crystals were obtained after 1 week for $\mathbf{2b}^{ox}$ and $\mathbf{2c}^{ox}$.

Preparation of $[\{[^nPr_2NH_2][Cr_7NiF_8(O_2C^tBu)_{15}(O_2C\text{-}py)]\}_2[Ru_2MO(^tBuCO_2)_6(py)]]$: M = Zn 3a, Ni 3b, and Co 3c

A solution of **2a**/**2b**/**2c** (0.022 g, 0.02 mmol) was added dropwise to a solution of **1** (0.100 g, 0.04 mmol) in acetone (15 mL), and the combined solution was stirred for 6 hr at 60°C. The purple solution was then filtered and kept at room temperature undisturbed until dark-brown crystals suitable for X-ray diffraction appeared.

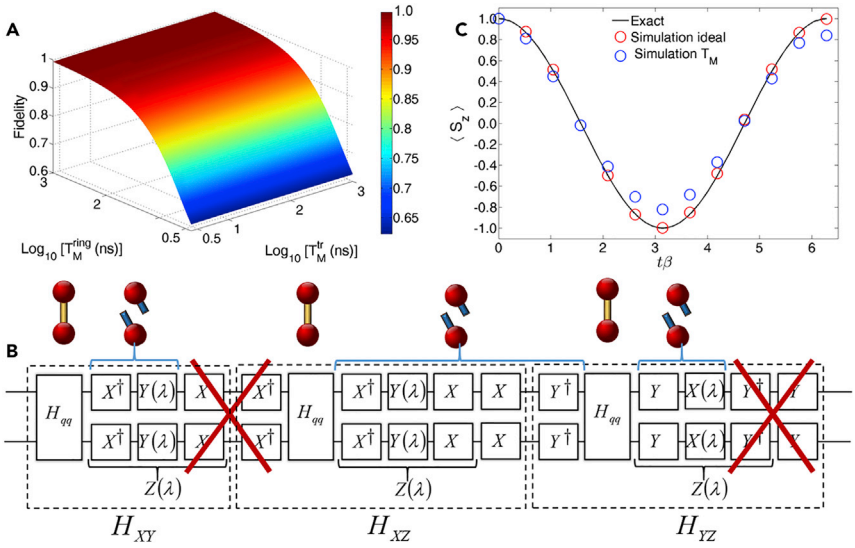

Figure 14. QIP with 3c

(A) Fidelity of the √iSWAP gate as a function of the phase memory time of the rings and of the triangular switch. The calculation was performed with a random initial state and application of a static field of 3 T.

(B) Quantum circuit for the digital quantum simulation of the Heisenberg model. H_{qq} is the free evolution with the switch in the "on" (reduced) state. The three blocks implementing H_{XY}, H_{XZ}, and H_{YZ} are enclosed within dashed boxes; for simplicity, we have introduced the notations $X = R_x(\pi/2)$, $Y = R_y(\pi/2)$, and $Z(\lambda) = R_z(\lambda)$. Consecutive direct and inverse unitary gates cancel each other out (red crosses). The two qubits are sketched as red spheres connected by the linker (switched on) or not (switched off) in the various steps of the evolution.

(C) Oscillations of the magnetization in the quantum simulation of Hamiltonian Equation 10; the system was initialized in a ferromagnetic configuration.

Preparation of [{[^{n}Pr$_2$NH$_2$][Cr$_7$NiF$_8$(O$_2$C^{t}Bu)$_{15}$(O$_2$C-py)]}$_2$[Ru$_2$MO(^{t}BuCO$_2$)$_6$(py)]]PF$_6$: M = Zn 3a^{ox}, Ni 3b^{ox}, and Co 3c^{ox}

Under an N_2 atmosphere, a dark-brown solution of **3a**/**3b**/**3c** (0.050 g, 0.009 mmol) in CH_2Cl_2 (5 mL) was combined with a 3 mM CH_2Cl_2 solution of [FeCp$_2$](PF$_6$) (3.0 mL, 0.009 mmol) and stirred for 30 min. The deep-purple solution was left to stand for 10 min before being filtered. Hexane (5 mL) was added, and the solution was concentrated to a third of the volume and placed in the freezer (−40°C) to crystallize. Unfortunately, just microcrystalline powder was obtained after several days for all compounds.

Single-Crystal X-Ray Diffraction

X-ray data were collected at a temperature of 100 K on an Oxford Instruments XCalibur2 X-ray diffractometer using MoKα radiation (λ = 0.71073 Å) for compounds **2b**, **2b′**, and **2c′** and equipped with an Oxford Cryosystems Cobra nitrogen flow gas system. X-ray data were collected at a temperature of 150 K on an Agilent Technologies Supernova diffractometer using MoKα radiation (λ = 0.71073 Å) for compounds **2a** and **2c** and equipped with an Oxford Cryosystems Cobra nitrogen flow gas system. Data were measured with the CrysAlisPro suite of programs. X-ray data for compounds **3b** and **3c** were collected at a temperature of 100 K with a Bruker X8 Prospector diffractometer using CuKα radiation (λ = 1.54184 Å) and equipped with an Oxford Cryosystems Cobra nitrogen flow gas system. Data were measured with the Bruker APEX2 suite of programs. Synchrotron X-ray data were collected at beamline I19 (λ = 0.6889 Å) Diamond Light Source[77] for compounds **2b**^{ox}, **2c**^{ox}, and **3a** at a temperature of 100 K. Data were measured with the CrystalClear-SM Expert 2.0 r5 suite of programs.

X-ray data for all the compounds were processed and reduced with the CrysAlisPro suite of programs. Absorption correction was performed via empirical methods based upon symmetry-equivalent reflections combined with measurements at different azimuthal angles.[78,79] The crystal structure was solved and refined against all F^2 values with the SHELXTL suite of programs.[80]

Pivalate ligands were disordered in all structures. The C–C distances were restrained with the SADI, DFIX, and SAME commands. The anisotropic displacement parameters were also restrained with SIMU, RIGU, and in some cases, EADP commands. Hydrogen atoms were placed in calculated positions, refined with idealized geometries (riding model), and assigned fixed isotropic displacement parameters.

Compounds **3b** and **3c** presented large voids filled with a lot of scattered electron density; the SQUEEZE protocol inside PLATON suites was used to account for the void electron density.[81]

Magnetic Measurements

Variable-temperature (2.0–300 K) direct-current magnetic-susceptibility measurements under an applied field of 1,000 G and variable-field (0–7.0 T) magnetization measurements at low temperatures (2.0 and 4 K) were carried out for **2a–3c** constrained in eicosane with a Quantum Design MPMS-XL7 SQUID magnetometer. The susceptibility data were corrected for the diamagnetism of the constituent atoms, the eicosane, and the sample holder. Fits were performed with the VPMAG package and PHI software.[82,83]

Electrochemical Measurements

Cyclic voltammograms were recorded with 0.1 M nNBu$_4$PF$_6$ as supporting electrolyte and 1.0 mM of **2a–3c** in dried dichloromethane. The working electrode was a glassy carbon disk (0.32 cm^2) that was polished with 1.0 μm diamond powder, sonicated, washed with absolute ethanol and acetone, and air dried. The reference electrode was AgClO$_4$/Ag separated from the test solution by a salt bridge containing the solvent and supporting electrolyte and platinum as the auxiliary electrode. All experiments were performed in standard electrochemical cells at 25°C under nitrogen. The investigated potential ranged from −2.00 to +1.80 V versus saturated calomel electrode (SCE). The formal potentials were measured at a scan rate of 50, 100, and 200 mV s^{-1}, and they were referred to the internal standard ferrocene/ferrocenium couple (E[Fc$^+$/Fc] = +0.46 V versus SCE; ΔE_p[Fc$^+$/Fc] = 80 mV; CH$_2$Cl$_2$, 0.1 M nBu$_4$NPF$_6$, 25°C).[84]

Spectroscopic Measurements

XANES spectra were measured at the Stanford Synchrotron Radiation Lightsource under ring conditions of 3.0 GeV and 300 mA. UV/visible-NIR spectra of solutions in dichloromethane at room temperature were recorded on a PerkinElmer Lambda 1050 spectrophotometer. X-band (ca. 9.5 GHz), K-band (ca. 24 GHz), Q-band (ca. 34 GHz), and W-band (ca. 94 GHz) EPR spectra were recorded with Bruker EMX580, Elexys 600, and EMX500 spectrometers at the UK Engineering and Physical Sciences Research Council National EPR Facility and Service at the University of Manchester. High-frequency and field EPR measurements were carried out at LNCMI Grenoble on a custom-built instrument.[85] Spectral simulations were performed with the EasySpin 4.5.5 simulation software.[86] Pulsed EPR measurements were performed at low temperatures on a Bruker ElexSys E580 spectrometer operating at X-band (ca. 9.5 GHz) and Q-band (ca. 34 GHz) frequencies. In all cases, dilute (0.0001 M) toluene solutions of compounds were used.

The inversion-recovery pulse sequence used was π-t-π/2-τ-π-τ-echo with π = 32 ns, τ = 320 ns, and variable *t*. The spin-lattice relaxation time constant, T_1, was deducted by fitting the resulting signal to Equation 11:

$$I(t) = I_1 \exp(-t/T_1) + I_{SD} \exp(-t/T_{SD}), \quad \text{(Equation 11)}$$

where I_1 and I_{SD} are the amplitudes and T_{SD} is the spectral diffusion time constant.

The spin-echo decay was measured by gradually increasing the inter-pulse delay τ of a primary Hahn echo sequence π/2-τ-π-τ-echo. With microwave pulses of length π = 32 ns, strong proton-electron spin modulation was observed. In order to suppress such modulation, microwave pulses of length π = 128 ns were used. The phase memory time T_M could be deducted by fitting the experimental data to Equation 12:

$$I(2\tau) = I(0)\exp[(-2\tau/T_M)^s], \quad \text{(Equation 12)}$$

where *s* is a stretching parameter.[11]

ACCESSION NUMBERS

The supplemental crystallographic data reported in this paper have been deposited in the Cambridge Crystallographic Data Center under accession numbers CCDC: 1415381–1415383, 1429637–1429641, and 1430001–1430002. These data are freely available via www.ccdc.cam.ac.uk/conts/retrieving.html (or from the Cambridge Crystallographic Data Center).

SUPPLEMENTAL INFORMATION

Supplemental Information includes Supplemental Experimental Procedures, 29 figures, 12 tables, and 1 data file and can be found with this article online at http://dx.doi.org/10.1016/j.chempr.2016.10.001.

AUTHOR CONTRIBUTIONS

Synthetic work was carried out by J.F.-S., S.A.M., G.F.S.W., and G.A.T. Crystallographic studies were performed by I.J.V.-Y. and G.F.S.W. Electrochemistry was performed by J.F.-S. EPR studies were performed by J.F.-S., F.T., and A.-L.B. XANES data were measured and interpreted by S.S. and K.M.L. Simulations of quantum gates were performed by A.C., S.C., and P.S. The project was devised by J.F.-S., R.E.P.W., S.C., and P.S. The manuscript was written by J.F.-S., A.C., and R.E.P.W. with significant input from the other authors.

ACKNOWLEDGMENTS

This work was supported by the UK Engineering and Physical Sciences Research Council (EPSRC) (studentships to S.A.M. and to G.F.S.W. through the CDT NoWNANO), the European Commission (Marie Curie Intra-European Fellowship to J.F.S. [622659]), and Excellence Unit "Maria de Maeztu" (MDM-2015-0538). We also thank the EPSRC for funding an X-ray diffractometer (grant number EP/K039547/1). We thank Diamond Light Source for access to synchrotron X-ray facilities. A.C., S.C., and P.S. acknowledge financial support from FIRB project no. RBFR12RPD1 of the Italian Ministry of Education and Research. K.M.L. thanks the National Science Foundation (CHE-1454455). We

thank the Stanford Synchrotron Radiation Lightsource for access to synchrotron X-ray facilities (DE-AC02-76SF00515 and P41GM103393).

Received: August 4, 2016
Revised: August 29, 2016
Accepted: October 3, 2016
Published: November 10, 2016

REFERENCES AND NOTES

1. Feynman, R.P. (1982). Simulating physics with computers. Int. J. Theor. Phys. *21*, 467–488.

2. Lloyd, S. (1996). Universal quantum simulators. Science *273*, 1073–1078.

3. Leuenberger, M., and Loss, D. (2001). Simulating physics with computers. Nature *410*, 789–793.

4. Sessoli, R., Tsai, H.L., Schake, A.R., Wang, S., Vincent, J.B., Folting, K., Gatteschi, D., Christou, G., and Hendrickson, D.N. (1993). High-spin molecules: [Mn12O12(O2CR) 16(H2O)4]. J. Am. Chem. Soc. *115*, 1804–1816.

5. Meier, F., Levy, J., and Loss, D. (2003). Quantum computing with spin cluster qubits. Phys. Rev. Lett. *90*, 47901–47904.

6. Troiani, F., Affronte, M., Carretta, S., Santini, P., and Amoretti, G. (2005). Proposal for quantum gates in permanently coupled antiferromagnetic spin rings without need of local fields. Phys. Rev. Lett. *94*, 190501.

7. Morita, Y., Yakiyama, Y., Nakazawa, S., Murata, T., Ise, T., Hashizume, D., Shiomi, D., Sato, K., Kitagawa, M., Nakasuji, K., and Takui, T. (2010). Triple-stranded metallo-helicates addressable as Lloyd's electron spin qubits. J. Am. Chem. Soc. *132*, 6944–6946.

8. Nakazawa, S., Nishida, S., Ise, T., Yoshino, T., Mori, N., Rahimi, R.D., Sato, K., Morita, Y., Toyota, K., et al. (2012). A synthetic two-spin quantum bit: *g*-engineered exchange-coupled biradical designed for controlled-NOT gate operations. Angew. Chem. Int. Ed. Engl. *51*, 9860–9864.

9. Lehmann, J., Gaita-Ariño, A., Coronado, E., and Loss, D. (2007). Spin qubits with electrically gated polyoxometalate molecules. Nat. Nanotechnol. *2*, 312–317.

10. Walsh, J.P.S., Meadows, S.B., Ghirri, A., Moro, F., Jennings, M., Smith, W.F., Graham, D.M., Kihara, T., Nojiri, H., Vitorica-Yrezabal, I., et al. (2015). Electronic structure of a mixed-metal fluoride-centered triangle complex: a potential qubit component. Inorg. Chem. *54*, 12019–12026.

11. Warner, M., Din, S., Tupitsyn, I.S., Morley, G.W., Stoneham, A., Gardener, J.A., Wu, Z., Fisher, A.J., Heutz, S., Kay, C.W.M., and Aeppli, G. (2013). Potential for spin-based information processing in a thin-film molecular semiconductor. Nature *503*, 504–508.

12. Graham, M.J., Zadrozny, J.M., Shiddiq, M., Anderson, J.S., Fataftah, M.S., Hill, S., and Freedman, D.E. (2014). Influence of electronic spin and spin–orbit coupling on decoherence in mononuclear transition metal complexes. J. Am. Chem. Soc. *136*, 7623–7626.

13. Bader, K., Dengler, D., Lenz, S., Endeward, B., Jiang, S.D., Neugebauer, P., and Slageren, J. (2014). Room temperature quantum coherence in a potential molecular qubit. Nat. Commun. *5*, 5304.

14. Zadrozny, J.M., Niklas, J., Poluektov, O.G., and Freedman, D.E. (2015). Millisecond coherence time in a tunable molecular electronic spin qubit. ACS Cent. Sci. *1*, 488–492.

15. Atzori, M., Tesi, L., Morra, E., Chiesa, M., Sorace, L., and Sessoli, R. (2016). Room-Temperature Quantum coherence and rabi oscillations in vanadyl phthalocyanine: toward multifunctional molecular spin qubits. J. Am. Chem. Soc. *138*, 2154–2157.

16. Pedersen, K.S., Ariciu, A.M., McAdams, S., Weihe, H., Bendix, J., Tuna, F., and Piligkos, S. (2016). Toward molecular 4f single-ion magnet qubits. J. Am. Chem. Soc. *138*, 5801–5804.

17. Aromí, G., Aguilà, D., Gamez, P., Luis, F., and Roubeau, O. (2012). Design of magnetic coordination complexes for quantum computing. Chem. Soc. Rev. *41*, 537–546.

18. Aguilà, D., Barrios, L.A., Velasco, V., Roubeau, O., Repollés, A., Alonso, P.J., Sesé, J., Teat, S.J., Luis, F., and Aromí, G. (2014). Heterodimetallic [LnLn′] lanthanide complexes: toward a chemical design of two-qubit molecular spin quantum gates. J. Am. Chem. Soc. *136*, 14215–14222.

19. Hanson, R., and Awschalom, D.D. (2008). Coherent manipulation of single spins in semiconductors. Nature *453*, 1043–1049.

20. Maurer, P.C., Kucsko, G., Latta, C., Jiang, L., Yao, N.Y., Bennett, S.D., Pastawski, F., Hunger, D., Chisholm, N., Markham, M., et al. (2012). Room-temperature quantum bit memory exceeding one second. Science *336*, 1283–1286.

21. Knowles, H.S., Kara, D.M., and Atatüre, M. (2014). Observing bulk diamond spin coherence in high-purity nanodiamonds. Nat. Mater. *13*, 21–25.

22. Wedge, C.J., Timco, G.A., Spielberg, E.T., George, R.E., Tuna, F., Rigby, S., McInnes, E.J.L., Winpenny, R.E.P., Blundell, S.J., and Ardavan, A. (2012). Chemical engineering of molecular qubits. Phys. Rev. Lett. *108*, 107204.

23. Morton, J.J.L., Tyryshkin, A.M., Ardavan, A., Porfyrakis, K., Lyon, S.A., and Briggs, G.A.D. (2005). High fidelity single qubit operations using pulsed electron paramagnetic resonance. Phys. Rev. Lett. *95*, 200501.

24. Shiddiq, M., Komijani, D., Duan, Y., Gaita-Ariño, A., Coronado, E., and Hill, S. (2016). Enhancing coherence in molecular spin qubits via atomic clock transitions. Nature *531*, 348–351.

25. Ardavan, A., Rival, O., Morton, J.J.L., Blundell, S.J., Tyryshkin, A.M., Timco, G.A., and Winpenny, R.E.P. (2007). Will spin-relaxation times in molecular magnets permit quantum information processing? Phys. Rev. Lett. *98*, 057201.

26. Mannini, M., Pineider, F., Danieli, C., Totti, F., Sorace, L., Sainctavit, Ph., Arrio, M.A., Otero, E., Joly, L., Cezar, J.C., et al. (2010). Quantum tunnelling of the magnetization in a monolayer of oriented single-molecule magnets. Nature *468*, 417–421.

27. Urdampilleta, M., Klyatskaya, S., Cleuziou, J.P., Ruben, M., and Wernsdorfer, W. (2011). Supramolecular spin valves. Nat. Mater. *10*, 502–506.

28. Ganzhorn, M., Klyatskaya, S., Ruben, M., and Wernsdorfer, W. (2013). Strong spin–phonon coupling between a single-molecule magnet and a carbon nanotube nanoelectromechanical system. Nat. Nanotechnol. *8*, 165–169.

29. Komeda, T., Isshiki, H., Katoh, K., and Yamashita, M. (2014). Variation of Kondo temperature induced by molecule–substrate decoupling in film formation of bis(phthalocyaninato)terbium(III) molecules on Au(111). ACS Nano *8*, 4866–4875.

30. Thiele, S., Balestro, F., Ballou, R., Klyatskaya, S., Ruben, M., and Wernsdorfer, W. (2014). Electrically driven nuclear spin resonance in single-molecule magnets. Science *344*, 1135–1138.

31. Cervetti, C., Rettori, A., Pini, M.G., Cornia, A., Repollés, A., Luis, F., Dressel, M., Rauschenbach, S., Kern, K., Burghard, M., and Bogani, L. (2016). The classical and quantum dynamics of molecular spins on graphene. Nat. Mater. *15*, 164–168.

32. Lehn, J.M. (1995). Supramolecular Chemistry: Concepts and Perspectives (Wiley-VCH).

33. Chakrabarty, R., Mukherjee, P.S., and Stang, P.J. (2011). Supramolecular coordination: self-assembly of finite two- and three-dimensional ensembles. Chem. Rev. *111*, 6810–6918.

34. Ward, M.D., and Raithby, P.R. (2013). Functional behaviour from controlled self-assembly: challenges and prospects. Chem. Soc. Rev. *42*, 1619–1636.

35. Santini, P., Carretta, S., Troiani, F., and Amoretti, G. (2011). Molecular nanomagnets as quantum simulators. Phys. Rev. Lett. *107*, 230502.

36. Troiani, F., Ghirri, A., Affronte, M., Carretta, S., Santini, P., Amoretti, G., Piligkos, S., Timco, G., and Winpenny, R.E.P. (2005). Molecular engineering of antiferromagnetic rings for quantum computation. Phys. Rev. Lett. *94*, 207208.

37. Chiesa, A., Whitehead, G.F.S., Carretta, S., Timco, G.A., Carthy, L., Teat, S.J., Amoretti, G., Pavarini, E., Winpenny, R.E.P., and Santini, P. (2014). Molecular nanomagnets with switchable coupling for quantum simulation. NPG Sci. Rep. *4*, 7423.

38. Ferrando-Soria, J., Fernandez, A., Moreno Pineda, E., Varey, S.A., Adams, R.W., Vitorica-Yrezabal, I.J., Tuna, F., Timco, G.A., Muryn, C.A., and Winpenny, R.E.P. (2015). Controlled synthesis of nanoscopic metal cages. J. Am. Chem. Soc. *137*, 7644–7647.

39. McInnes, E.J.L., Timco, G.A., Whitehead, G.F.S., and Winpenny, R.E.P. (2015). Heterometallic rings: their physics and use as supramolecular building blocks. Angew. Chem. Int. Ed. Engl. *54*, 14244–14269.

40. Carretta, S., Santini, P., Amoretti, G., Guidi, T., Copley, J.D.R., Qiu, Y., Caciuffo, R., Timco, G., and Winpenny, R.E.P. (2007). Quantum oscillations of the total spin in a heterometallic antiferromagnetic ring: evidence from neutron spectroscopy. Phys. Rev. Lett. *98*, 167401.

41. Trif, M., Troiani, F., Stepanenko, D., and Loss, D. (2008). Spin-electric coupling in molecular magnets. Phys. Rev. Lett. *101*, 217201.

42. Sasaki, Y., Suzuki, M., Tokiwa, A., Ebihara, M., Yamaguchi, T., Kabuto, C., and Ito, T. (1988). Bis(μ-acetato)($\mu-$oxo)-bis(tris(pyridine) ruthenium(III)) ion: a ruthenium analog of the hemerythrin active center. J. Am. Chem. Soc. *110*, 6251–6252.

43. Sasaki, Y., Suzuki, M., Nagasawa, A., Tokiwa, A., Ebihara, M., Yamaguchi, T., Kabuto, C., Ochi, T., and Ito, T. (1991). Preparation, structure, and properties of the bis(μ-acetato)(μ-oxo)ruthenium(III) dimers $[Ru_2(\mu\text{-}CH_3COO)_2(\mu\text{-}O)(py)_6]^{2+}$ and $[Ru_2(\mu\text{-}CH_3COO)_2(\mu\text{-}O)(bpy)_2(py)_2]^{2+}$. Inorg. Chem. *30*, 4903–4908.

44. Adaption of the synthesis of manganese pivalate with zinc acetate as a starting material Kiskin, M.A., Fomina, I.G., Aleksandrov, G.G., Sidorov, A.A., Novotortsev, V.M., Rakitin, Y.V., Dobrokhotova, Z.V., Ikorskii, V.N., Shvedenkov, Y.G., Eremenko, I.L., et al. (2005). New antiferromagnetic Mn(II) pivalate polymer: synthesis and reactivity. Inorg. Chem. Commun. *8*, 89–93.

45. Aromí, G., Batsonov, A.S., Christian, P., Helliwell, M., Parkin, A., Parsons, S., Smith, A.A., Timco, G.A., and Winpenny, R.E.P. (2003). Synthetic and structural studies of cobalt–pivalate complexes. Chem. Eur. J. *9*, 5142–5161.

46. Sasaki, Y., Tokiwa, A., and Ito, T. (1987). Mixed ruthenium-rhodium trinuclear complex $[Ru_2Rh(\mu_3\text{-}O)(CH_3COO)_6(L)_3]^+$ (L = H_2O or pyridine). J. Am. Chem. Soc. *109*, 6341–6347.

47. Kobayashi, H., Uryû, N., Miyamoto, R., Ohba, Y., Iwaizumi, M., Sasaki, Y., Ohto, A., and Ito, T. (1995). Magnetic properties of some triangular trinuclear complexes of $[Ru_2M(\mu\text{-}CH_3COO)_6(\mu_3\text{-}O)(py)_3]^{n+}$ with a diamagnetic ion M. Bull. Chem. Soc. Jpn. *68*, 2551–2558.

48. Kobayashi, H., Uryû, N., Mogi, I., Miyamoto, R., Ohba, Y., Iwaizumi, M., Sasaki, Y., Ohto, A., Suwabe, M., and Ito, T. (1996). Magnetic properties of some triangular trinuclear complexes of $[Ru_2M(\mu\text{-}CH_3COO)_6(\mu_3\text{-}O)(py)_3]^{n+}$ with a paramagnetic ion M. Bull. Chem. Soc. Jpn. *69*, 3163–3172.

49. Abe, M., Tanaka, M., Makhosi, K., and Sasaki, Y. (1999). Enhanced kinetic lability of Ru(III) centers in oxo-centered mixed-metal Ru_2M trinuclear complexes (M = Zn and Mg). Inorg. Chem. *38*, 4116–4148.

50. Cannon, R.D., and White, R.P. (1988). Chemical and physical properties of triangular bridged metal complexes. Prog. Inorg. Chem. *36*, 195–298.

51. Kobayashi, H., Uryû, N., Tokiwa, A., Yamaguchi, T., Sasaki, Y., and Ito, T. (1992). Magnetic properties of oxygen centered trinuclear ruthenium(III) and rhodium(III) complexes. Bull. Chem. Soc. Jpn. *65*, 198–202.

52. Earnshaw, A., Figgis, B.N., Lewis, J., and Peacock, R.D. (1961). The magnetic properties of some d^4-complexes. J. Chem. Soc. *1961*, 3132–3138.

53. Dunbar, K.R., Shelter, E.J., Palii, A.V., Ostrovsky, S.M., Mirovitskii, V.Y., Hudson, J.M., Omari, M.A., Klokishner, S.I., and Tsukerblat, B.S. (2003). Unusual magnetic behavior of six-coordinate, mixed-ligand Re(II) complexes: origin of a strong temperature-independent paramagnetism. J. Phys. Chem. A *107*, 11102–11111.

54. Magee, S.A., Sproules, S., Barra, A.L., Timco, G.A., Chilton, N.F., Collison, D., Winpenny, R.E.P., and McInnes, E.J.L. (2014). Large zero-field splittings of the ground spin state arising from antisymmetric exchange effects in heterometallic triangles. Angew. Chem. Int. Ed. Engl. *53*, 5310–5313.

55. Dzyaloshinski, I. (1958). A thermodynamic theory of "weak" ferromagnetism of antiferromagnetics. J. Phys. Chem. Sol. *4*, 241–255.

56. Moriya, T. (1960). New mechanism of anisotropic superexchange interaction. Phys. Rev. Lett. *4*, 228–230.

57. Tsukerblat, B.S., Kuyavskaya, B.Y., Belinskii, M.I., Ablov, A.V., Novotortsev, V.M., and Kalinnikov, V.T. (1975). Antisymmetric exchange in the trinuclear clusters of copper(II). Theoret. Chim. Acta *38*, 131–138.

58. Tsukerblat, B. (2008). Group-theoretical approaches in molecular magnetism: metal clusters. Inorg. Chim. Acta *361*, 3746–3760.

59. Boca, R., and Herchel, R. (2010). Antisymmetric exchange in polynuclear metal complexes. Coord. Chem. Rev. *254*, 2973–3025.

60. Ferrer, S., Lloret, F., Pardo, E., Clemente-Juan, J.M., Liu-González, M., and García-Granda, S. (2012). Antisymmetric exchange in triangular tricopper(II) complexes: correlation among structural, magnetic, and electron paramagnetic resonance parameters. Inorg. Chem. *51*, 985–1001.

61. Lloret, F., Julve, M., Cano, J., Ruiz-García, R., and Pardo, E. (2008). Magnetic properties of six-coordinated high-spin cobalt(II) complexes: theoretical background and its application. Inorg. Chim. Acta *361*, 3432–3445.

62. Dul, M.C., Pardo, E., Lescouëzec, R., Chamoreau, L.M., Villain, F., Journaux, Y., Ruiz-García, R., Cano, J., Julve, M., Lloret, F., et al. (2009). Redox switch-off of the ferromagnetic coupling in a mixed-spin tricobalt(II) triple mesocate. J. Am. Chem. Soc. *131*, 14614–14615.

63. Ottenwaelder, X., Aukauloo, A., Journaux, Y., Carrasco, R., Cano, J., Cervera, B., Castro, I., Curreli, S., Muñoz, M.C., Roselló, A.L., et al. (2005). Synthesis, structure, spectroscopy and redox chemistry of square-planar nickel(II) complexes with tetradentate *o*-phenylenedioxamidates and related ligands. Dalton Trans. 2516–2526.

64. Cotton, F.A., and Norman, J.G., Jr. (1972). Structural characterization of a basic trinuclear ruthenium acetate. Inorg. Chim. Acta *6*, 411–419.

65. Baumann, J.A., Salmon, D.J., Wilson, S.T., Meyer, T.J., and Hatfield, W.E. (1978). Electronic structure and redox properties of the clusters $[Ru_3O(CH_3CO_2)_6L_3]^{n+}$. Inorg. Chem. *17*, 3342–3350.

66. Tanase, T., Takeshita, N., Inoue, C., Kato, M., Yano, S., and Sato, K. (2001). Diruthenium complexes with hydrotris(1-pyrazolyl)borate face-capping ligands involving {Ru_2(μ-O or μ-OH)(μ-carboxylato)$_2$} cores. J. Chem. Soc. Dalton Trans. 2293–2302.

67. Sudha, C., Mandal, S.K., and Chakravarty, A.R. (1998). Synthesis, X-ray structures, and spectroscopic and electrochemical properties of (μ-oxo)bis(μ-carboxylato)diruthenium complexes having six imidazole bases as terminal ligands. Inorg. Chem. *37*, 270–278.

68. Suzuki, T., Matsuya, K., Kawamoto, T., and Nagao, H. (2013). Synthesis and structures of mixed-valence oxido-bridged diruthenium complexes bearing ethylbis(2-pyridylmethyl) amine. Eur. J. Inorg. Chem. *4*, 722–727.

69. Piligkos, S., Weihe, H., Bill, E., Neese, F., El Mkami, H., Smith, G.M., Collison, D., Rajaraman, G., Timco, G.A., Winpenny, R.E.P., and McInnes, E.J.L. (2009). EPR spectroscopy of a family of $Cr^{III}_7M^{II}$ (M = Cd, Zn, Mn, Ni) "wheels": studies of isostructural compounds with different spin ground states. Chem. Eur. J. *15*, 3152–3167.

70. Fernandez, A., Moreno Pineda, E., Muryn, C.A., Sproules, S., Moro, F., Timco, G.A., McInnes, E.J.L., and Winpenny, R.E.P. (2015). *g*-Engineering in hybrid rotaxanes to create AB and AB_2 electron spin systems: EPR spectroscopic studies of weak interactions between dissimilar electron spin qubits. Angew. Chem. Int. Ed. Engl. *54*, 10858–10861.

71. Ferrando-Soria, J., Moreno Pineda, E., Chiesa, A., Fernandez, A., Magee, S.A., Carretta, S., Santini, P., Vitorica-Yrezabal, I.J., Tuna, F., Timco, G.A., et al. (2016). A modular design of molecular qubits to implement universal quantum gates. Nat. Commun. *7*, 11377.

72. Fei, J., Zhou, D., Shim, Y.-P., Oh, S., Hu, X., and Friesen, M. (2012). Mediated gates between spin qubits. Phys. Rev. A *86*, 062328.

73. Las Heras, U., Mezzacapo, A., Lamata, L., Filipp, S., Wallraff, A., and Solano, E. (2014). Digital quantum simulation of spin systems in superconducting circuits. Phys. Rev. Lett. *112*, 200501.

74. Vincent, R., Klyatskaya, S., Ruben, M., Wernsdorfer, W., and Balestro, F. (2012). Electronic read-out of a single nuclear spin using a molecular spin transistor. Nature *488*, 357–360.

75. Burzurí, E., Zyazin, A.S., Cornia, A., and van der Zant, H.S.J. (2012). Direct observation of magnetic anisotropy in an individual Fe_4 single-molecule magnet. Phys. Rev. Lett. *109*, 147203.

76. Corradini, V., Ghirri, A., Garlatti, E., Biagi, R., De Renzi, V., del Pennino, U., Bellini, V., Carretta, S., Santini, P., Timco, G., et al. (2012). Magnetic anisotropy of Cr_7Ni spin clusters on surfaces. Adv. Funct. Mat. *22*, 3706–3713.

77. Nowell, H., Barnett, S.A., Christensen, K.E., Teat, S.J., and Allan, D.R. (2012). I19, the small-molecule single-crystal diffraction beamline at Diamond Light Source. J. Synchrotron Radiat. *19*, 435–441.

78. Sheldrick, G.M. (1995). SADABS, Empirical Absorption Correction Program Based upon the Method of Blessing (University of Göttingen).

79. Blessing, R.H. (1995). An empirical correction for absorption anisotropy. Acta Crystallogr. *A51*, 33–38.

80. Sheldrick, G.M. (2015). A short history of SHELX. Acta Crystallogr. *A71*, 3–8.

81. PLATON, A. (2008). Multipurpose Crystallographic Tool (Utrecht University).

82. Cano, J. (2003). VPMAG Package (University of Valencia).

83. Chilton, N.F., Anderson, R.P., Turner, L.D., Soncini, A., and Murray, K.S. (2013). PHI: a powerful new program for the analysis of anisotropic monomeric and exchange-coupled polynuclear d- and f-block complexes. J. Comput. Chem. *34*, 1164–1175.

84. Connelly, N.G., and Geiger, W.E. (1996). Chemical redox agents for organometallic chemistry. Chem. Rev. *96*, 877–910.

85. Barra, A.L., Brunel, L.C., and Robert, J.B. (1990). EPR spectroscopy at very high field. Chem. Phys. Lett. *165*, 107–109.

86. Stoll, S., and Schweiger, A. (2006). EasySpin, a comprehensive software package for spectral simulation and analysis in EPR. J. Magn. Reson. *178*, 42–55.